October 2019

Vanadium-based Nanomaterials for Improved Zn Ion Storage

Jianwei Lai
Louisiana State University and Agricultural and Mechanical College

VANADIUM-BASED NANOMATERIALS FOR IMPROVED ZN ION STORAGE

A Thesis

Submitted to the Graduate Faculty of the
Louisiana State University and
Agricultural and Mechanical College
in partial fulfillment of the
requirements for the degree of
Master of Science in Mechanical Engineering

in

The Department of Mechanical & Industrial Engineering

by
Jianwei Lai
B.S., South China University of Technology, 2017
December 2019

Acknowledgements

First, I would like to express my great appreciation and respect to my advisor, Prof. Ying Wang for her continuous guidance, encouragement, and support on my research projects. The significant guidance from Prof. Wang leads me to the research on electrochemical energy storage and conversion.

I am very thankful to Prof. Dorel Moldovan and Prof. Manas Gartia for serving as my committee members and their indispensable help. I also want to sincerely thank my collaborators, Dr. Zhiqiang Xie, Dr. Wangwang Xu, Dr. Xiuping Zhu, Dr. Qinglin Wu, and Dr. Xiuxuan Sun at Louisiana State University (LSU).

Table of Contents

Abstract

Rechargeable aqueous zinc-ion batteries (ZIBs) have been intensively studied as novel promising large-scale energy storage systems recently, owing to their advantages of high abundance, cost effectiveness, and high safety. However, the development of suitable cathode materials with superior performance are severely hampered by the sluggish kinetics of Zn^{2+} with divalent charge in the host structure.

Our Work demonstrates boosting the electrochemical performances of nanostructured cathode materials for aqueous ZIBs. The first project is focused on the interlayer-expanded $V_6O_{13}{\cdot}nH_2O$ nanosheets as promising cathodes. Benefiting from the synthetic merits of its favorable architecture and expanded interlamellar spacing resulted from its structural water, the $V_6O_{13}{\cdot}nH_2O$ cathode exhibits outstanding electrochemical performances with a high reversible capacity of 395 mAh g^{-1} at 0.1 A g^{-1}, superior rate capability, and durable cycling stability with a capacity retention of 87% up to 1000 cycles. In addition, the reaction mechanism is significantly investigated in detail. Moreover, the second project is focused on the synthesis of $NH_4V_3O_8{\cdot}1.9H_2O$ nanobelts and investigation of the electrochemical properties in aqueous and quasi-solid-state (QSS) ZIBs. When examined in aqueous ZIBs, this cathode material enables ultrafast Zn^{2+} diffusion and highly reversible process, exhibiting superior electrochemical performances with a high discharge capacity of 463 mAh g^{-1} at 0.1 A g^{-1}, excellent rate capability (183 mAh g^{-1} even at 10 A g^{-1}), and impressive cycling stability with a capacity retention of 81% after 2000 cycles maintaining a decent discharge capacity of 166 mAh g^{-1} at 10 A g^{-1}. Furthermore, the $NH_4V_3O_8{\cdot}1.9H_2O$ electrode can deliver a high energy density of 332 Wh kg^{-1} at a power density of 72 W kg^{-1} and maintain an energy density of 101 Wh kg^{-1} at a high power density of 5519 W kg^{-1}. The $NH_4V_4O_{10}{\cdot}1.6H_2O$ is also studied as cathode materials for aqueous ZIBs, showing

inferior electrochemical properties when compared with $NH_4V_3O_8 \cdot 1.9H_2O$. In addition, the QSS flexible Zn/$NH_4V_3O_8 \cdot 1.9H_2O$ battery is also studied, showing durable cycling performance and stable electrochemical properties under various bending states.

The present studies demonstrate that the $V_6O_{13} \cdot nH_2O$ nanosheets and $NH_4V_3O_8 \cdot 1.9H_2O$ nanobelts are emerging as high-potential cathode materials for rechargeable zinc-ion battery, and it sheds light on the rational design of novel cathodes for grid-scale energy storage devices.

1. Introduction

1.1. General Background of Zinc Ion Batteries

The increasing demands for environmentally friendly large-scale energy storage devices with high energy density, high safety, and low cost have stimulated the development of advanced rechargeable batteries, due to the energy crisis and environmental pollution caused by traditional energy technology.[1-2] Among various energy storage systems, lithium-ion batteries (LIBs) have been widely used in portable electrical devices and large-scale energy storage systems for several decades.[3-4] However, the high cost, limited lithium resources, as well as safety concerns on flammable organic electrolytes greatly hinder their further development.[5-6] Recently, rechargeable multivalent ion (Zn^{2+}, Mg^{2+}, Ca^{2+}, or Al^{3+}) batteries have been attracting great interests, considered as both high-potential and high-safety energy storage devices when compared to expensive and unsafe Li-ion batteries.[7-8] In this regard, rechargeable aqueous ZIBs are particularly attractive due to their distinctive advantages, such as low cost, low redox potential of Zn^{2+}/Zn (-0.76 V vs. standard hydrogen electrode), high abundance, high stability in water, high theoretical capacity (820 mAh g^{-1}) as well as high energy density (5851 mAh mL^{-1}) in terms of zinc metals.[9] The cost and environmental pollution can be greatly reduced by replacing traditional organic electrolytes with aqueous-based electrolytes. Such aqueous electrolytes can exhibit excellent ionic conductivity up to 1.0 S cm^{-1}, superior to the organic electrolytes, and may effectively boost the high rate capabilities of aqueous ZIBs for grid-scale renewable energy storage systems.[10-11] As shown in Figure 1.1, the aqueous ZIBs are constructed by three main parts, including cathode materials, aqueous electrolyte, and metallic zinc foil anode. There is a separator between cathode and anode. During the discharge process, zinc ions migrate and intercalate into the cathode. During the charge process, the intercalated zinc ions would extract from cathode materials.

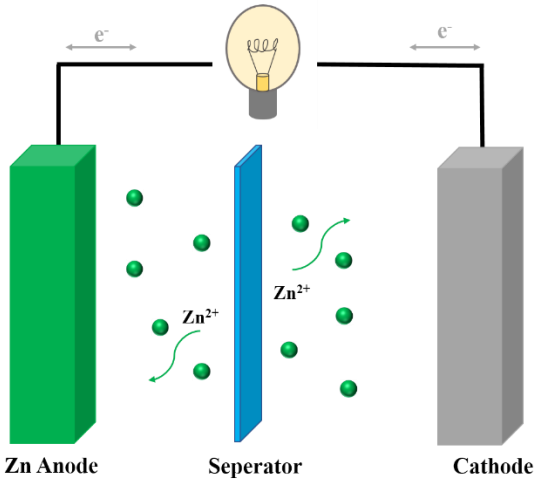

Figure 1.1. Schematic illustration of aqueous ZIBs.

In addition, the every-growing demands for flexible devices have promoted the development of wearable energy storage applications. Flexible QSS rechargeable batteries with unique mechanical properties are capable of being bent, folded, or rolled without sacrificing their excellent electrochemical performances. Such QSS batteries have beneficial impacts on a wide set of flexible applications, such as medical devices (e.g., diagnosis) and smart devices (e.g., wearable electronics).[12] As a competitive candidate, rechargeable QSS ZIBs show numerous advantages, such as electrolyte-leak prevention compared to the liquid counterparts, good compatibility with human body, cost effectiveness, and intrinsic safety. Furthermore, the Zn^{2+} based QSS electrolytes offer desirable flexibility, high stability, and effectively eliminate the formation of zinc dendrites, showing high potential for flexible energy storage devices.[13]

As a proof of concept, a smart wire-shaped flexible zinc-ion battery with shape memory function was designed for improved electrochemical performances, flexibility, and wearable properties, by utilizing the temperature-initiated shape memory effect.[14] The gel polymer electrolyte is fabricated by employing gelatin and borax in aqueous solution of $ZnSO_4/MnSO_4$, and it presents higher ionic conductivity of 2.0×10^{-2} S cm^{-1} compared to the bare gelatin gel

electrolyte with 1.39×10^{-2} S cm^{-1}. Owing to the introduction of borax as a cross-linker into the gelatin gel electrolyte, the ionic conductivity, water retention capability, and mechanical strength of the gelatin-borax gel electrolyte are effective improved, thereby enhancing the electrochemical performances of the zinc-ion battery. Such flexible wire battery exhibits a specific capacity of 174.2 mAh g^{-1} at 0.5 C and durable cycling performance up to 1000 cycles with corresponding coulombic efficiencies over 99%. Additionally, its electrochemical performance can be well preserved when bent to 90° or consecutively bent to 45° for over 500 cycles, indicating its superior resistance against mechanical deformation.

Searching for a stable sulfate-tolerant polymer electrolyte without polymer precipitation, Li *et al.* explored a xanthan bio-polymer in combination with aqueous $ZnSO_4/MnSO_4$ solution to fabricate a very stable gum bio-electrolyte, which was then assembled in a rechargeable Zn/MnO_2 battery for electrochemical characterizations.[15] Owing to its favorable molecular structure composed of α,β-1,4-linked glucan backbone with trisaccharide side chains connected with backbone residues by α-1,3 linkages, the xanthan gum shows high salt-tolerance stability. The as-synthesized gum bio-electrolyte is highly conductive (1.46×10^{-2} S cm^{-1} at room temperature and 2.5×10^{-3} S cm^{-1} at -8 °C), and its ionic conductivity remains unchanged even after one-year storage, indicating its ability of working in a wide temperature range and long-term stability. As a result, this battery presented a specific capacity of 260 mAh g^{-1} at 1 C, high rate capability, good cycling performance with 90% capacity retention after 330 cycles at 1 C, and even maintained a decent capacity of 127 mAh g^{-1} up to 1000 cycles at 5 C. Moreover, the battery cell exhibits outstanding durability under bending and twisting, and effectively prohibits the zinc dendrites growth during continuous charge-discharge cycles, suggesting the gum bio-electrolyte is a very promising candidate for flexible and wearable energy storage systems.

Another quasi-solid-state zinc-ion battery with high rate capability and high stability was reported recently, using a layered zinc orthovanadate array (ZOV array) as cathode, a Zn array as anode, a gel electrolyte composed of fumed silica with aqueous $ZnSO_4$ solution.[16] This battery displays superior electrochemical behaviors and ultra-stable flexibility. Specifically, the flexible cell exhibits a highly reversible capacity of 204 mAh g^{-1} with an initial high Coulombic efficiency of 95% at 0.5 C, corresponding to a 2 electrons transfer process. Due to the nanoarray structure in both electrodes providing short fast ion migration pathways and introduced insertion pesudocapacitance, the quasi-solid-state battery delivers an excellent rate capability of 160 mAh g^{-1} at 10 C and 101 mAh g^{-1} even at 50 C. Furthermore, the quasi-solid-state zinc-ion battery shows long-term cycling stability for 2000 cycles at 20 C, and considerable energy density of 115 Wh kg^{-1} with a power density of 5.1 kW kg^{-1} based on the total masses of cathode, anode, and current collectors. Additionally, the battery reveals no obvious capacity fading with over 96% capacity retention under continuous 100 bending cycles, showing it can tolerate bending without deterioration of the discharge performance.

Zhi *et al.* also developed a flexible self-healing solid-state aqueous rechargeable NiCo/Zn battery by employing NiCo hydroxide as cathode, flexible Zn/carbon cloth as anode, and Fe^{3+}-crosslinking sodium polyacrylate (PANa-Fe^{3+}) hydrogel as solid-state electrolyte.[17] Owing to the Fe^{3+} crosslinkers forming ionic bonds between the PANa chains, and the favorable compatibility of PANa-Fe^{3+} with aqueous solution of $Zn(CH_3COO)_2$ + KOH, the as-prepared self-healing electrolyte displays enhanced healing property and good ionic conductivity. As a result, the assembled NiCo/Zn battery with such intrinsically self-healing PANa-Fe^{3+} electrolyte shows autonomically self-healing ability with over 87% capacity retention after 4 cycles of cutting/healing. When the two broken part of the cell were brought to connect, the watch was on

again without weakening the brightness, implying the excellent healing performance and high potential for its practical application in broken electronics.

Very recently, a flexible Zn/MnO_2 battery was constructed and displayed exceptionally electrochemical performances, operating at subzero temperatures.[18] Hydrogel electrolytes are promising candidates as solid-state electrolyte for flexible ZIBs. However, the freezing issue of hydrogel electrolytes under subzero temperatures would lead to severe capacity fading and elasticity loss. Moreover, the mechanical robustness and flexibility cannot maintain under such harsh temperature condition. In this work, the strong hydrogen bonding with water anchored the water units within the as-fabricated polymer electrolyte, rendering superior anti-freezing property even at -20℃. The constructed Zn/MnO_2 flexible battery maintained high electrochemical performances, impressive durability, and flexibility even being compressed, bent, or washed in an ice bath at -20℃. Such excellent polymer electrolyte may boost the development of practical applications in flexible ZIBs under some extreme condition, such as aerospace or submarines.

1.2. Typical Cathode Materials for Zinc Ion Batteries

Recently, intensive research in designing the advanced materials of ZIBs have been conducted for large-scale energy storage.[7] Significant efforts and investigations have contributed to the rapid development of reversible zinc-ion storage electrode materials, such as manganese-based oxides, Prussian blue analogs, and vanadium-based materials. Manganese oxides, including α-, β-, γ-, and δ-MnO_2 have been studied as intercalation hosts for zinc ion.[19-22] Unfortunately, MnO_2 suffers from poor rate performance and rapid capacity fading in aqueous electrolyte. For example, Kim *et al.* reported a δ-MnO_2 nanoflake cathode with a capacity of 252 mAh g^{-1}, and only 44% of the highest capacity can be retained after 100 cycles at 83 mAh g^{-1}.[22] Liu *et al.* reported

a ZIB with improved energy density and cycling performance by employing $MnSO_4$ as additive for the effective suppression of Mn^{2+} when cycling.[23] Attempts on the Prussian blue analogs delivered limited capacity (~50 mAh g^{-1}), and suffered from O_2 evolution at a high operation voltage of ~1.7 V.[24]

The advantages of vanadium-based materials for ZIBs include high specific capacity, high safety, abundance resource, and low cost. Layered vanadium oxide bronzes show enhanced cycling stability and rate capability by employing cations or structural water as "pillars".[25-27] These "pillars" can effectively improve the structural stability during charge-discharge process and provide a fast Zn^{2+} diffusion path. Mai *et al.* presented a $V_2O_5 \cdot nH_2O$/graphene cathode with expanded interlayer spacing (1.26 nm) for ZIBs, which delivered a high specific capacity of ~372 mAh g^{-1} at 0.3 A g^{-1} and retained 71% of the maximum capacity after 900 cycles at 6 A g^{-1}.[28] It should be noted that the intercalation kinetics of Zn^{2+} in metal oxides are sluggish due to the intensive polarization and large solvation sheath of Zn^{2+}. Such good electrochemical performance of the $V_2O_5 \cdot nH_2O$/graphene cathode can be attributed to the reduced effective charge in H_2O-solvated Zn^{2+}.

Nazar *et al.* developed a $Zn_{0.25}V_2O_5 \cdot nH_2O$ pillared by Zn^{2+} and crystalline water. The Zn ions "pillars" in $Zn_{0.25}V_2O_5 \cdot nH_2O$ can stabilize this layered structure, contributing to its cycling stability. Notably, owing to the crystal water and inserted Zn^{2+}, such stable layered structure could buffer the volume change caused by the intercalation of Zn^{2+} with divalent charge during the discharge process. As expected, the integral ZIBs exhibited a decent capacity of ~282 mAh g^{-1} at 0.3 A g^{-1} and 81% capacity retention after 1000 cycles at 2.4 A g^{-1}.[25]

Moreover, a scalable and green synthesis strategy was employed for the preparation of a series of vanadate nanobelts, including $NaV_3O_8 \cdot 1.35H_2O$ (NVO), $Zn_3V_2O_8 \cdot 1.85H_2O$ (ZnVO), and

$KV_3O_8 \cdot 0.51H_2O$ (KVO).[27] The NVO, ZnVO, and KVO displayed high capacities of 366, 328, and 316 mAh g^{-1} at the same current density of 0.1 A g^{-1}. Their rate capabilities were further investigated, presenting considerable capacities of ~100 mAh g^{-1} at an extremely high current density of 10 A g^{-1}. Notably, under 10 A g^{-1}, NVO exhibited the first discharge capacity of 186 mAh g^{-1} with maintained capacity of 200 mAh g^{-1} over 200 cycles, while ZnVO displayed an initial capacity of 205 mAh g^{-1} with restored capacity of 191 mAh g^{-1} after 200 cycles. The XRD results coupling with XPS characterization of NVO electrodes at the initial, discharged, and charged states confirmed the highly reversible Zn2+ insertion/extraction in the electrodes, which contributed to the favorable long-term cycling stability. This study provided a large-scale production method for promising vanadates cathode with high capacities and durable stability for next-generation aqueous ZIBs.

Mai *et al.* also reported a sodium stabilized vanadium oxide ($Na_{0.33}V_2O_5$) nanowire cathode, showing a capacity of 367.1 mAh g^{-1} at 0.1 A g^{-1} and 93% capacity retention could be achieved after 1000 cycles at 1 A g^{-1}.[29] Kim *et al.* constructed a LiV_3O_8 cathode with a capacity of ~256 mAh g^{-1} at 16 mAh g^{-1} and 75% capacity retention after 65 cycles at 133 mA g^{-1}.[30] Liang *et al.* studied a variety of sodium vanadates, demonstrating that $Na_5V_{12}O_{32}$ displayed a high capacity of 281 mAh g^{-1} at 0.5 A g^{-1} and maintained 71% capacity over 2000 cycles at 4 A g^{-1}.[31] They also investigated $NH_4V_4O_{10}$ cathode with ~ 400 mAh g^{-1} at 0.3 A g^{-1} with negligible capacity loss up to 1000 cycles at 10 A g^{-1}.[32] Except for few cathode candidates, most reported cathode materials of ZIBs are seriously hindered by the low specific capacity, poor rate capability and limited cycle life for future practical applications.[8] Therefore, it is an urgent need to develop a novel vanadium-based oxide cathode material with high capacity, high durability, and excellent rate performance, which may play a crucial role in the breakthrough of achieving practical large-scale ZIBs.

Very recently, a $Co_{0.247}V_2O_5 \cdot 0.944H_2O$ cathode with high-voltage output and long-term cycling life was reported.[33] A series of CV measurements with various scan rates were studied. The calculated b values of peak 1 to 4 were 0.86, 0.77, 0.92, and 0.78, indicating partial capacitive contribution. Remarkably, the integral cell provided a impressive capacity of 432 mAh g^{-1} at 0.1 A g^{-1} and 163 mAh g^{-1} at 10 A g^{-1}, rendering outstanding rate performance. By employing first principles study, the diffusion energy barrier of $Co_{0.247}V_2O_5 \cdot 0.944H_2O$ was much lower than $V_2O_5 \cdot nH_2O$, suggesting the $Co_{0.247}V_2O_5 \cdot 0.944H_2O$ showed a faster kinetics. The cycling property was further investigated at 4 A g^{-1}, displaying over 90% capacity retention for 7500 cycles. In comparison with published electrodes in aqueous ZIBs, such $Co_{0.247}V_2O_5 \cdot 0.944H_2O$ electrode provided both the highest energy density and power density. The favorable electrochemical performances were attributed to the stable crystal structure, fast kinetics, and desired adsorption capability for Zn^{2+}.

1.3. Objectives of the Thesis

To significantly improve the electrochemical properties of rechargeable ZIBs including specific capacity, long-term cycling stability, and rate capability for large-scale energy storage systems, this study explored two layered vanadium-based nanomaterials ($V_6O_{13} \cdot nH_2O$ and $NH_4V_3O_8 \cdot 1.9H_2O$) as high-performance electrodes for aqueous and QSS ZIBs.

Owing to its high specific capacity, wide availability, and low cost, the reaction mechanism and electrochemical performance of mixed-valence V_6O_{13} have been explored in organic electrolytes for rechargeable alkali-ion-based batteries.[34-35] For instance, Yu *et al.* reported the V_6O_{13} nanotextiles evaluated as a cathode for LIBs, which delivered a high capacity of 326 mAh g^{-1} at 20 mA g^{-1} and a reversible capacity of 134 mAh g^{-1} at 500 mA g^{-1} respectively, showing the

superior electrochemical performance and huge potential as high-energy cathode materials.[34] Based on the first principle calculations, previous study reveals that the water insertion in interlayer-expanded $V_6O_{13}{\cdot}nH_2O$ is ascribed to the strong intercalation of water molecules and the lattice O ions between the single and double layers, forming hydroxyl radicals on each side. Such expanded interlayer spacing by water intercalation exhibited good rate capability and excellent cycling stability for lithium ion storage.[36] Moreover, V_6O_{13} with the mixed valences of V^{4+} and V^{5+} shows high electronic conductivity at room temperature, which is favorable for the ultrafast charge and discharge process when applied in the battery system.[34] Therefore, hydrated V_6O_{13} is expected to be a promising electrode material for zinc ion storage, showing high potential for industrial production and superior electrochemical activity.

The electrochemical property of $NH_4V_3O_8$ was investigated in rechargeable Li^+ ion batteries. For instance, Liu *et al.* published the $NH_4V_3O_8$ nanorod cathode for use in LIBs that presented a high capacity of ~ 327 mAh g^{-1} at 0.03 A g^{-1} and impressive rate performance with a reversible capacity of 181.8 mAh g^{-1} at 0.6 A g^{-1} respectively.[37] Notably, the large interlayer spacings of $NH_4V_3O_8$ is 8.1 Å, which is easily accessible for Zn^{2+} transportation, which may become the competitive electrode candidate for superior ZIBs.

Herein, the first objective includes the investigation of Zn^{2+} storage performances by employing $V_6O_{13}{\cdot}nH_2O$ nanosheets as cathode materials, Zn metal as anode, and aqueous $Zn(CF_3SO_3)_2$ solution as the electrolyte. The critical role of structural water is emphasized by comparing the electrochemical behaviors between $V_6O_{13}{\cdot}nH_2O$ and V_6O_{13}. In addition, the corresponding reaction mechanism is studied by analyzing the crystal structure of samples at various charge-discharge states from X-ray Diffraction (XRD) characterization. The second objective includes the study of electrochemical properties of $NH_4V_3O_8{\cdot}1.9H_2O$ nanobelts as

cathodes for aqueous and quasi-solid-state zinc ion batteries. By coupling XRD and X-ray photoelectron spectroscopy (XPS), the superior zinc ion storage capability of $NH_4V_3O_8 \cdot 1.9H_2O$ cathodes with stable "pillars" (e.g., NH_4^+, H_2O) is elucidated and investigated.

1.4. Thesis Overview

Chapter 1 introduces the literature review about rechargeable zinc ion batteries, including the aqueous and quasi-solid-state electrolytes as high-potential electrolytes for practical energy storage applications. The typical cathode materials with various electrochemical behaviors and physical-chemical properties for zinc ion storage are also introduced in the chapter.

Chapter 2 describes the preparation of interlayer-expanded hydrated V_6O_{13} via hydrothermal synthesis for enhanced aqueous zinc ion storage. The crystal structure, morphologies, and lattice water content are investigated by XRD, SEM/TEM, and TGA. Employing cyclic voltammetry (CV) and galvanostatic charge-discharge method, the electrochemical performances between $V_6O_{13} \cdot nH_2O$ and dehydrated V_6O_{13} are examined and compared. Moreover, the electrochemical reaction mechanism of $V_6O_{13} \cdot nH_2O$ is studied through a series of XRD patterns of $V_6O_{13} \cdot nH_2O$ electrodes at different charged/discharged states.

Chapter 3 describes the layered $NH_4V_3O_8 \cdot 1.9H_2O$ emerging as high-potential cathode materials for superior aqueous and quasi-solid-state zinc ion batteries. The crystal structure, morphologies, and lattice water content of $NH_4V_3O_8 \cdot 1.9H_2O$ are investigated by XRD, SEM/TEM, and TGA, respectively. The CV measurements, rate capabilities and long-term cycling of $NH_4V_3O_8 \cdot 1.9H_2O$ cathodes using aqueous or quasi-solid-state electrolytes are carefully studied. The fundamental mechanism for the excellent electrochemical properties is examined by quantifying the charge storage kinetics through CV method, galvanostatic intermittent titration

technique, and electrochemical impedance spectroscopy. In addition, the electrochemical behaviors of the constructed quasi-solid-state flexible Zn/ $NH_4V_3O_8 \cdot 1.9H_2O$ battery under different bending states are evaluated.

Chapter 4 summarizes the main conclusions on the rational design of vanadium-based nanomaterials for enhanced zinc ion storage. The future perspective about zinc ion batteries is also provided and discussed.

2. Interlayer-Expanded $V_6O_{13}{\cdot}nH_2O$ Architecture Constructed for Advanced Rechargeable Aqueous Zinc Ion Battery

2.1. Experimental Section

$V_6O_{13}{\cdot}nH_2O$ was synthesized by modifying a previous method.[36] In a typical synthesis, 0.15 M commercial V_2O_5 powder and 0.45 M $H_2C_2O_4$ were first added into 40 mL deionized water, and then the above mixture was stirred at 90 °C for 1 h to obtain a dark blue solution. Then, the above solution was transferred into a 100 mL Teflon-lined autoclave. Later, 10 mL hydrogen peroxide and 30 mL ethanol were added to the above solution in sequence and kept at 180 °C for 3 h. Finally, the product, $V_6O_{13}{\cdot}nH_2O$ (H-VO) was collected, washed with deionized water and ethanol several times, and then dried at 60 °C in vacuum overnight. The control sample, V_6O_{13} (VO) was obtained through annealing the H-VO at 400 °C under Ar gas flow for 2 h.

The XRD data were collected at a constant scanning rate of 2° min^{-1} on a Rigaku MiniFlex X-ray diffractometer with Cu Kα radiation (λ = 1.5405 Å). Scanning electron microscopy (SEM) imaging was carried out on a FEI Quanta 3D FEG field emission scanning electron microscopy (FESEM), equipped with Energy-dispersive X-ray spectroscopy (EDS). Transmission electron microscopy (TEM) and high-resolution TEM (HRTEM) imaging was performed on a JEOL JEM-2010 microscope at 200 kV. Thermogravimetry (TG) data were collected using an SII STA7300 analyzer under the nitrogen atmosphere.

Electrochemical measurements were performed with 2032 coin-type cells assembled in air. The working electrode was fabricated by rolling 60 wt% active material, 30 wt% conductive carbon (Super P), and 10 wt% polytetrafluoroethylene (PTFE) into thin film. The active materials

mass loading is ~7.2 mg cm^{-2}. Zinc foil, 3 M zinc trifluoromethanesulfonate ($Zn(CF_3SO_3)_2$) aqueous solution, and glass fiber membrane were used as the anode, electrolyte, and separator, respectively. Galvanostatic charge-discharge experiments were carried out on an eight-channel battery analyzer (MTI corporation) with a voltage range of 0.2- 1.4 V. Cyclic voltammetry measurements were conducted on an electrochemical workstation (CHI 6504C) at different scan rates. High current charge-discharge, galvanostatic intermittent titration technique (GITT) measurements were operated on a potentiostat (VMP3, Bio-Logic). Before the GITT measurement, the assembled cell was first discharged and charged at 100 mA g^{-1} for one cycle to obtain a stable state. Subsequently, the assembled cell was discharged or charged at 50 m g^{-1} for 0.5 h, and then relaxed for 1 h to make the voltage reach the equilibrium. The procedure was repeatedly applied to the cell during the entire charge-discharge process until reaching to the cut-off voltage.

2.2. Results and Discussion

H-VO nanosheets were synthesized via a simple hydrothermal method and the proposed synthesis mechanism is presented in Figure A1. Briefly, vanadium oxide powder first fully reacted with oxalic acid in a molar ratio of 1: 3 to form a homogeneous vanadyl oxalate hydrate ($VOC_2O_4 \bullet nH_2O$) solution, and the color of the solution simultaneously turned to dark blue. Then the H-VO was successfully fabricated through the reaction between the generated VO^{2+} species and hydrogen peroxide.[36] The morphology of as-synthesized H-VO was studied by SEM and TEM. As shown in Figure 2.1a, the H-VO displays a hollow microflower structure with sizes of 2-7 μm. The high-resolution SEM image further presents that these hollow structures are constructed by two-dimensional ultra-thin nanosheets with widths of 50-200 nm, which are entangled together (Figure 2.1b). In addition, the presences of V, O, and C in H-VO are confirmed in the EDS results,

showing a carbon content of ~2.99 wt% (Figure A2). Furthermore, the TEM image in Figure 2.1c shows that the H-VO possesses ultra-thin layers feature, consistent with the high-solution SEM image. From the high-resolution TEM image in Figure 2.1d, a single nanosheet exhibits distinct lattice fringe areas apart from areas without fringe, and it could be attributed to the carbon layer covered on the surface of the nanosheet, which was formed during the hydrothermal reaction. It should be noted that such in situ coating of carbon on the surface of the H-VO nanosheets would be beneficial to enhance the interfacial conductivity of the sample when evaluated in aqueous ZIB. The interplanar spacing of 0.583 nm is well matched with the (200) crystalline facet of H-VO. Such favorable hollow structure of H-VO would be advantageous for the fast kinetics of Zn^{2+} intercalation and deintercalation. In order to determine the crystalline water content of H-VO, TGA was carried out in the temperature range of 30-500 °C under the nitrogen atmosphere as displayed in Figure 2.1e. The total weight loss is attributed to the evaporation of physically absorbed water (30-100 °C) and lattice water (100-350 °C). Based on a weight loss of 3.5 wt%, it can be estimated that there is approximately 1.1 structural water per V_6O_{13} unit. The crystal structure of the as-prepared H-VO was characterized by XRD as presented in Figure 2.1f. The XRD pattern of H-VO can be well indexed to monoclinic V_6O_{13} with the space group of C2/m (unit cell parameters of a = 11.9 Å, b = 3.671 Å, c = 10.122 Å, and $\beta = 100.87°$; JCPDS no. 01-072-1278). Based on Bragg's equation ($d=0.5n\lambda/\sin\theta$), the diffraction peak located at lower angles indicates a larger interlayer distance. The diffraction peak of H-VO at $2\theta = 7.8°$ from facet (001) is attributed to the water insertion with expanded interlayer, and the corresponding interlayer spacing is calculated to be 1.13 nm, which is larger than 0.99 nm at $2\theta = 8.9°$ from the standard PDF card. The larger lattice spacing of 1.13 nm may provide more diffusion channels for the migration of Zn^{2+}, and the expanded interlamellar spacing is comparable to the $V_2O_5 \cdot nH_2O$ cathode,[28] more

electrochemically superior to previous reported VS_2,[40] Zinc Pyrovanadate,[38] and $Na_2V_6O_{16}\cdot 3H_2O$,[39] etc. In addition, the expanded interlayer of H-VO at (001) plane is in good agreement with the previous report.[36] After annealing at 400 °C under Ar flow for 2 h, the dehydrated V_6O_{13} (VO) is obtained. The diffraction peak attributed to the interlayer spacing of 1.13 nm is divided into two peaks at 9.1° and 12.4°, indicating the decreased lattice space. The peak position change suggests that the interlayer expansion is mainly attributed to the water intercalation.

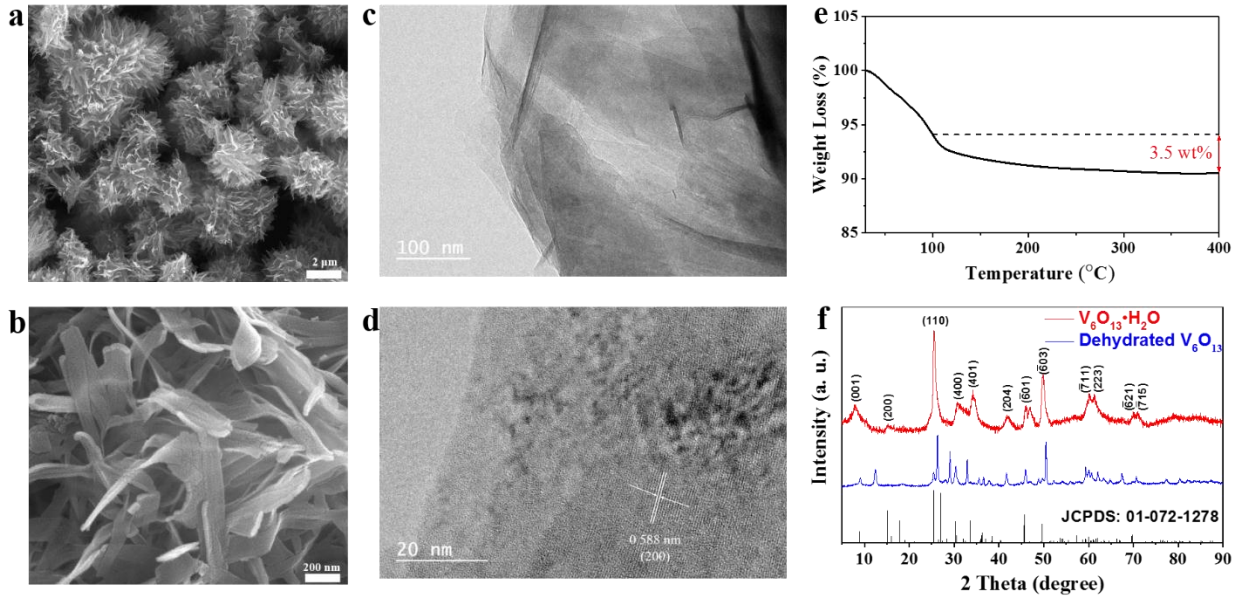

Figure 2.1. (a-b) SEM images of the as-synthesized H-VO. (c-d) TEM and HRTEM images of H-VO. (e) Corresponding TGA result of H-VO. (f) Powder XRD patterns of H-VO and VO.

The electrochemical performances of H-VO and VO as cathode materials were evaluated using 3 M $Zn(CF_3SO_3)_2$ aqueous solution as electrolyte and metallic zinc foil as anode assembled in 2032 coin-type cells. The initial three cyclic voltammogram (CV) curves of H-VO in the voltage range of 0.2-1.4 V (*vs.* Zn/Zn^{2+}) at a scan rate of 0.1 mV s^{-1} are displayed in Figure 2.1a. During the first cathodic scan, there are five cathode perks located at 1.07, 0.90, 0.76, 0.63, and 0.44 V, and the small peak at 1.07 V may be caused by some irreversible reactions occurring in the initial

cycle, which will be discussed later. The remaining four cathode peaks are slightly different from the peak positions at 0.91, 0.77, 0.65, and 0.46 V in the subsequent cycles of reduction scan. The reduction peak shifting could be ascribed to the activation of H-VO during discharge process. From the initial three anodic scans, they exhibit completely overlapping peaks at 0.52, 0.78, 0.95, and 1.10 V. In addition, the CV curves in the initial three cycles show good similarity and repeatability with the exclusion of a small deviation in the first cathodic CV curves, suggesting the good structural stability and excellent reversibility of the Zn/H-VO battery. Over four distinct pairs of reduction/oxidation peaks are clearly observed, implying a four-step reaction mechanism corresponding to the Zn^{2+} insertion/extraction. Such CV curves of the H-VO are quite different from many reported vanadium-based cathodes for aqueous ZIBs with only two pairs of redox peaks, such as $V_2O_5 \cdot nH_2O$,[28] $Zn_2V_2O_7$,[40] and $H_2V_3O_8$.[41] For VO electrode, five reduction peaks of the first cathodic scan at 1.10, 0.78, 0.62, 0.56, and 0.50 V are noticeably different from three cathode peaks at 0.85, 0.65, and 0.49 V in the following two cycles, and three oxidation peaks at 0.59, 0.76, and 1.00 V can be observed in these initial three cycles (Figure A3a). Furthermore, the selected second CV curves comparison at 0.1 mV s^{-1} between H-VO and VO show significant differences based on the number of peaks and corresponding peak positions (Figure A3b).

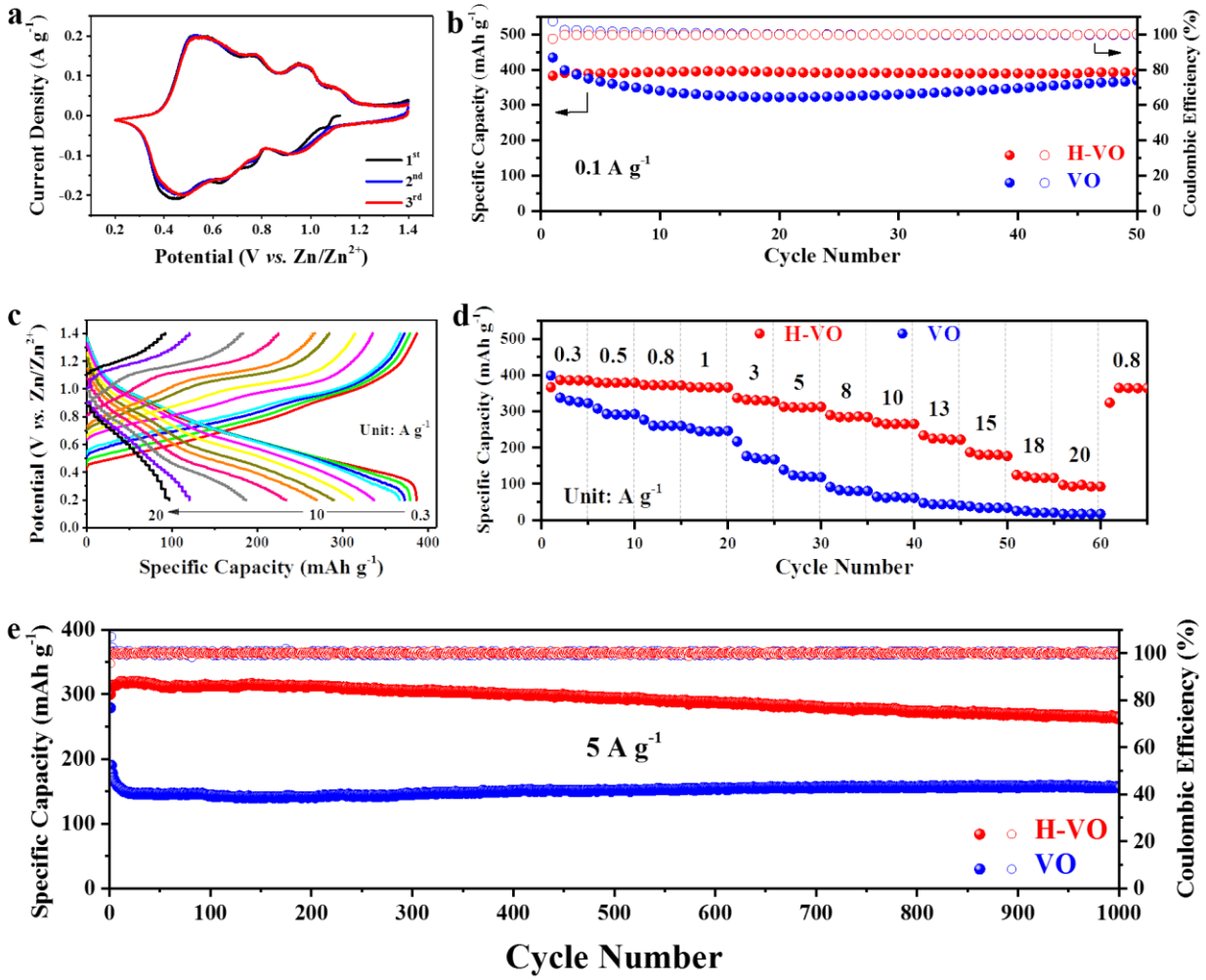

Figure 2.2. Electrochemical performances of the H-VO and VO electrodes within the potential range of 0.2- 1.4 V *vs.* Zn/Zn^{2+}. (a) CV curves of H-VO electrode at a scan rate of 0.1 mV s^{-1} in the initial three cycles. (b) Cycling performance and the corresponding coulombic efficiency of H-VO and VO electrodes at 0.1 A g^{-1}. (c) Galvanostatic charge-discharge profiles of H-VO electrode under various current density. (d) Rate capabilities of H-VO and VO electrodes. (e) Long-term cycling properties of H-VO and VO electrodes at 5 A g^{-1}.

Based on such highly reversible CV curves of these two cathodes, their cycling performances are further investigated by employing the galvanostatic charge-discharge method. As presented in Figure 2.2b, H-VO delivers a remarkable and stable initial discharge capacity of 383 mAh g^{-1} at a current density of 0.1 A g^{-1}, and corresponding charge capacity of 392 mAh g^{-1} with a high initial coulombic efficiency of 97.6%. The favorable coulombic efficiency implies good reversibility of Zn^{2+} ingress/egress. In the following 15 cycles, the specific capacity gradually

increases which is ascribed to the activation process of the H-VO electrode, and then stabilizes in the range of 390-395 mAh g^{-1} with an overall coulombic efficiency over 99.5%. It should be noted that the H-VO can maintain the high and stable capacities of ~390 mAh g^{-1} when applied a low current density of 0.1 A g^{-1} during the whole 50 cycles, which outperforms many previous reported cathodes that suffered from severe capacity fade under the same current density in the initial few cycles,[29, 38, 41] indicating the high reversibility and stability nature of the H-VO electrode. Based on the high discharge capacity of 390 mAh g^{-1}, the number of electrons transfer during electrochemical reaction is calculated to be ~7.7, corresponding to 3.85 Zn^{2+} migration. Notably, the vanadium ions in H-VO can be reduced to V^{3+} with 8 electrons transfer, so its theoretical capacity can be calculated to be 401.6 mAh g^{-1}. As discussed above, the CV curves of H-VO electrode show multistep Zn^{2+} intercalation/deintercalation behaviors (Figure 2.3a). According to Figure 2.4c, H-VO delivers a capacity of 104.2 mAh g^{-1} at 0.3 A g^{-1} in the voltage range of 0.8-1.4 V during the discharge process, corresponding to one Zn^{2+} (two electrons transfer) insertion. Subsequently, H-VO displays a capacity of 278.8 mAh g^{-1} in 0.2-0.8 V, corresponding to ~2.77 Zn^{2+} (5.54 electrons transfer) intercalation. Notably, there are two V^{5+} and four V^{4+} ions for each $V_6O_{13}{\cdot}1.1H_2O$. Therefore, we speculate that two V^{5+} ions are reduced to V^{4+} (2 electrons transfer) during 0.8-1.4 V, and 5.54 V^{4+} are further reduced to V^{3+} (5.54 electrons transfer) during 0.2-0.8 V. Similarly, H-VO presents a capacity of 282.8 mAh g^{-1} between 0.2 and 0.93 V during charge process, corresponding to the oxidation of 5.63 V^{3+} to V^{4+}. In the voltage range of 0.93-1.4 V, a capacity of 104.3 mAh g^{-1} is shown, relevant to the oxidation of 2 V^{4+} to V^{5+}. Thus, 5.63 V^{3+} are oxidized to V^{4+} during 0.2-0.93 V, and 2 V^{4+} are oxidized to V^{5+} during 0.93-1.4 V. It should be noted that H-VO exhibits a discharge capacity of 211 mAh g^{-1} during 0.6-1.4 V, and a discharge capacity of 175.6 mAh g^{-1} during 0.2-0.6 V at 0.3 A g^{-1}, which shows ~54.6% capacity contribution

in 0.6-1.4 V, and 45.4% (＜50%) capacity is obtained in 0.2-0.6 V (Figure 2.5c). These results are similar to the previously reported VOG sample having a capacity contribution of 59% in 0.6-1.6 V and 41% in 0.2-0.6 V.[28] However, for the dehydrate VO electrode, although it provides a higher first discharge capacity of 434 mAh g^{-1} at the same current density of 0.1 A g^{-1} due to the elimination of structural water, VO displays a significantly reduced initial charge capacity of 404 mAh g^{-1}, indicating a poorly reversible process. The capacity of VO dramatically decreases to 323 mAh g^{-1} when further charge-discharge after 20 cycles, and then gradually increases to 370 mAh g^{-1}, which may be ascribed to the activation and stabilization of VO by water intercalation and irreversible Zn^{2+} as pillars trapped in the interlayer during cycling. Such relatively unstable cycling performance of VO largely hinders its practicability for grid-scale energy storage devices. Moreover, the comparison of typical galvanostatic charge-discharge curves at the selected cycle with a current density of 0.1 A g^{-1} between H-VO and VO manifests a reversibly high capacity of ~395 mAh g^{-1} is achieved for H-VO, while an unfavorable capacity of ~323 mAh g^{-1} is presented for VO (Figure A4).

Furthermore, the excellent rate performance is of significance for large-scale aqueous ZIBs to address the ever-growing demands for practical energy storage systems. However, many previous reported cathodes for aqueous ZIBs display undesirable rate behaviors, which are largely hampered by the high polarization of Zn^{2+} with divalent charge in the host structure. In the presented H-VO electrode, it shows exceptionally satisfactory capacity even under severe galvanostatic test. The comparison of rate capabilities and corresponding charge-discharge curves with a voltage range of 0.2-1.4 V starting from a current density of 0.3 to 20 A g^{-1} are illustrated in Figure 2.6c-d. Extraordinarily, via increasing the current density from 0.3 up to 10 A g^{-1}, the H-VO electrode exhibits impressive capacities of 386 and 270 mAh g^{-1} respectively with only ~30%

capacity loss. Even applied the highest current rate of 20 A g^{-1}, a considerable capacity of 97 mAh g^{-1} still can be obtained. The corresponding discharge or charge time is as short as ~17.5 s, demonstrating ultrafast charge transfer kinetics of the H-VO electrode and superior rate capability. More importantly, as the current density abruptly returns back to 0.8 A g^{-1}, the reversible discharge capacity restores to 364 mAh g^{-1}, which is comparable to the specific capacity of 372 mAh g^{-1} under the same current density in previous cycles, manifesting a strong endurance for rapid Zn^{2+} insertion/extraction and good structural reversibility. In contrast, the rate behavior of VO applied with identical increasing current rates is severely inferior, displaying an initial discharge capacity of 398 mAh g^{-1} at 0.3 A g^{-1} and drastically declining to 61 mAh g^{-1} at 10 A g^{-1} with corresponding capacity fading over 80%, and further to 16 mAh g^{-1} at 20 A g^{-1} (Figure 2.7d and Figure A5). Such significant rate performance difference implies that the water intercalation in H-VO plays a vital role in remarkably improving the rate capability. The superior capacities of H-VO under a series of current densities probably benefit from the enlarged interlamellar spacing (1.13 nm), which provides abundant accessible channels, and simultaneously facilitates rapid transportation of electrolyte ions through the electrode. In addition, the unique hollow-microflower structure of H-VO assembled from ultra-thin nanosheets can not only effectively shorten the diffusion path lengths of Zn^{2+} ingress/egress, but also possess the volume flexibility to buffer the volume change during cycling. Furthermore, H-VO with mixed valance states of V^{4+} and V^{5+} shows metallic characteristics, which can increase the electrical conductivity of the electrode, and enable the fast electron transfer. Therefore, the excellent rate performance of Zn/H-VO battery could not only realize high capacity, but also achieve ultrafast charge/discharge process.

The long-term cycling properties at a high current density of 5 A g^{-1} are further examined to reveal the superiority of H-VO as opposed to VO in Figure 2.8e and Figure A6. H-VO delivers

an initial desirable discharge capacity of 300 mAh g^{-1}, with a corresponding high coulombic efficiency over 95%. Benefiting from the water incorporation synthetic strategy, H-VO can impressively maintain a high capacity of 262 mAh g^{-1} even after 1000 cycles with a capacity retention of 87% under the critical high current density, and the correlative high coulombic efficiencies over 99% are achieved except for the first cycle. Furthermore, a marked distinction in cycle life between H-VO and VO is clearly observed, showing that the average capacity of H-VO is 292 mAh g^{-1}, while VO only displays 151 mAh g^{-1} average capacity. The significant gap is as large as 141 mAh g^{-1}, almost comparable to the average capacity of VO. Such magnificent cycling performance should be attributed to the unique architecture of H-VO cathode, where the expanded interlayer at plane (001) through the successful introduction of structural water facilitates Zn^{2+} diffusion. Based on the synthetic merits of H-VO, it exhibits more durable cycling stability without adding any vanadium sol in the electrolyte or graphene support as compared to the $V_2O_5 \cdot nH_2O$/graphene cathode for aqueous ZIB.[28]

The electrochemical kinetics of the H-VO electrode are further investigated through CV measurements and the galvanostatic intermittent titration technique (GITT).[42] Figure A7a presents the CV profiles of the H-VO electrode at the scan rate of 0.1 mV s^{-1} and 0.2 mV s^{-1}. There are four pairs redox peaks at 0.1 mV s^{-1} as discussed above. When the scan rate increases to 0.2 mV s^{-1}, the CV curves show two pairs of distinct redox peaks, and the other two small redox peaks become broad due to the larger scan rate. The capacitive response can be calculated by employing the equation of $i = av^b$, where both a and b are adjustable parameters. This equation can be rearranged to $\log i = b \log v + \log a$. The coefficient b of ~0.5 represents a diffusion control process, while b of ~1 indicates a capacitive process. As shown in Figure A7b, the relationships between log *i* and log *v* are plotted, and the b values of the four peaks are determined to be 0.92, 1.20, 1.06, and

0.83 respectively, which suggests that the charge storage behaviors are mainly controlled by pseudocapacitive process. Furthermore, the ratio of capacitive contribution can be decided by the equation of $i = k_1v + k_2v^{1/2}$ at a specific potential, where k_1v is capacitive effect and $k_2v^{1/2}$ represents diffusion control process. At the scan rate of 0.1 mV s^{-1}, ~62.9% capacity is attributed to the capacitive process, which implies the capacitive contribution is dominant. This 62.9% capacitive contribution of the H-VO electrode is comparable to 61.4% contribution in the previously reported VS_2 at the same scan rate.[43] Moreover, the Zn^{2+} diffusion coefficient (D_{Zn}^{2+}) can be calculated based on the following equation:

$$D_{Zn^{2+}} = \frac{4L^2}{\pi\tau}\left(\frac{\Delta E_s}{\Delta E_t}\right)^2 \quad (1)$$

where L is the diffusion length (cm) of Zn^{2+} which is equal to the thickness of electrode, τ is the relaxation time (s), ΔEs is the steady-state potential change (V) by the current pulse during a single-step GITT experiment. ΔEt represents the potential change (V) during the constant current pulse of a single-step GITT experiment after eliminating the iR drop. As displayed in Figure 2.9, the overall calculated diffusion coefficients of Zn^{2+} (D_{Zn}^{2+}) during the entire discharge process in the H-VO cathode are higher than the D_{Zn}^{2+} in VO cathode, demonstrating the faster kinetics of as-synthesized H-VO electrode. The average D_{Zn}^{2+} of H-VO in the discharge process are 1.3 times larger than that of VO. The higher ionic diffusivity of H-VO is ascribed to its enlarged lattice spacing (1.13 nm in 001), which can not only provide more effective diffusion path for Zn^{2+} migration but also effectively reduce the electrostatic interactions in the crystal structure of H-VO during the electrochemical intercalation process. It is worth noting that the Zn^{2+} diffusion coefficients of H-VO in the graph under different insertion states keep stable except for the fully intercalation state, indicating the excellent stability of its structure during the ingress of Zn^{2+}. The lower D_{Zn}^{2+} when approaching 0.2 V results from the increased electrostatic repulsion in the H-

VO electrode upon Zn^{2+} insertion. The above GITT analysis result can convincingly support the superior rate capability and remarkable cycling stability of the H-VO electrode instead of VO.

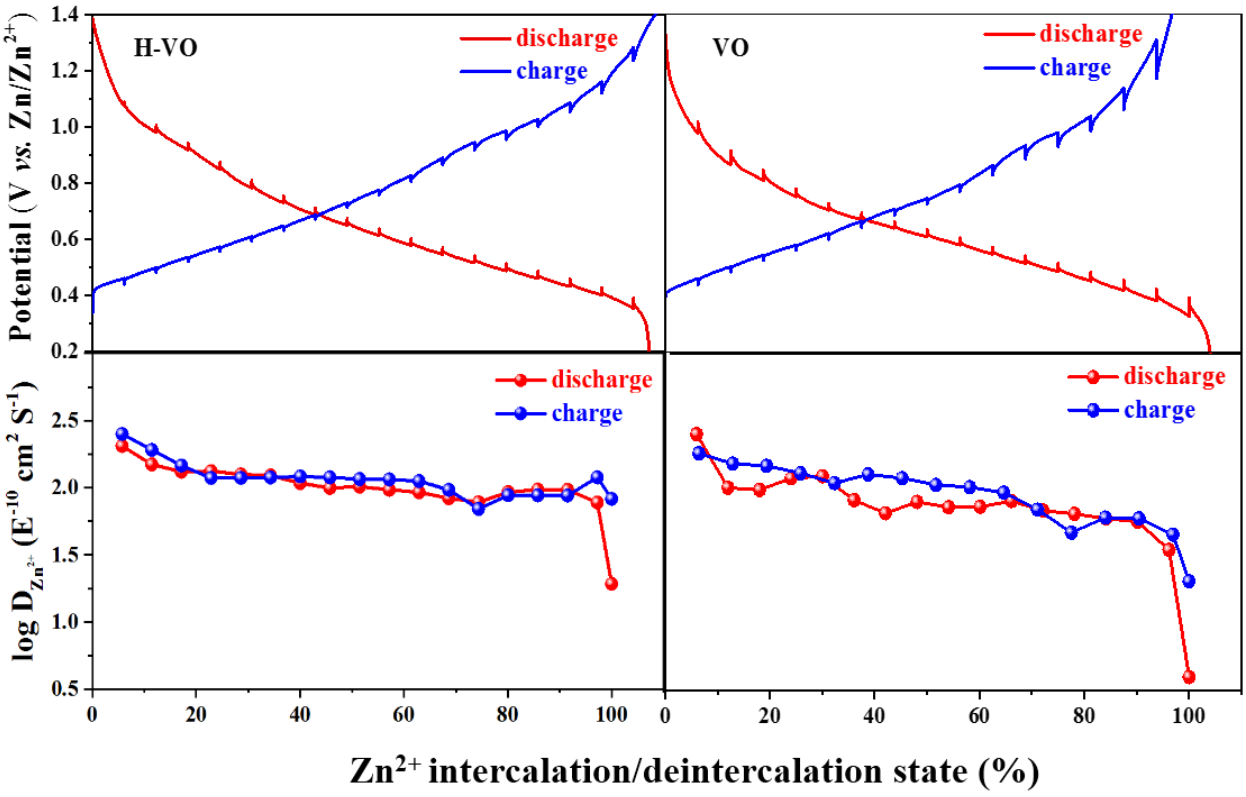

Figure 2.3. GITT curves and calculated diffusion coefficient of Zn^{2+} vs. various Zn^{2+} insertion/extraction states of H-VO and VO.

The outstanding Zn^{2+} intercalation/deintercalation performance of the H-VO electrode is further reflected in comparison to previously reported vanadium-based cathodes for aqueous ZIBs. As presented in Table A1, our developed H-VO electrode demonstrates the highest specific capacity of 395 mAh g^{-1}, and the superlative retained capacity of 262 mAh g^{-1} with an impressive capacity retention over 87%, which outperforms these published cathode materials, showing its high potential for practical energy storage devices.

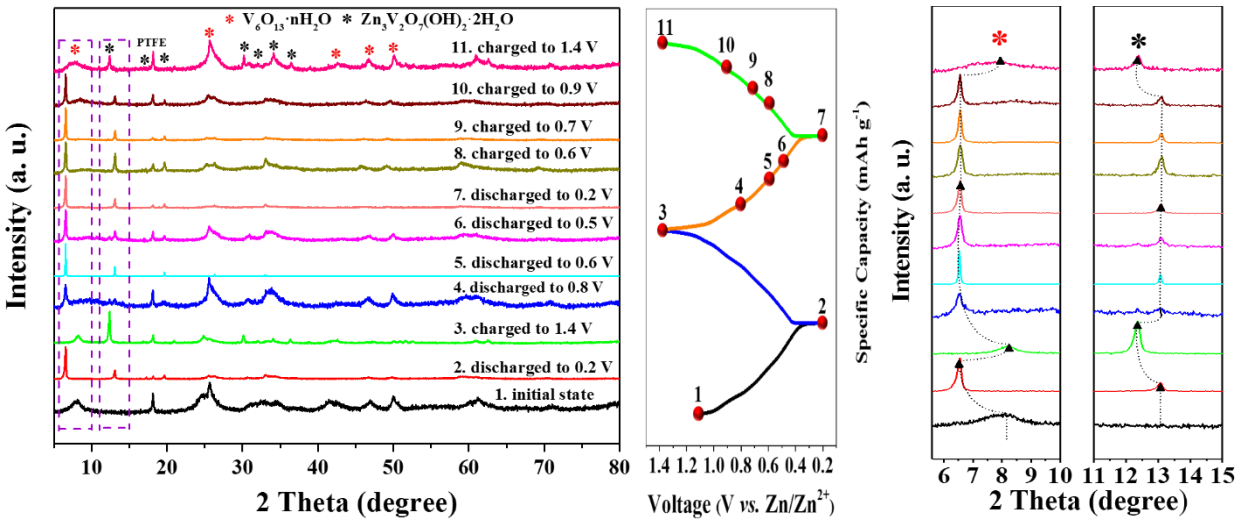

Figure 2.4. Ex situ XRD patterns of H-VO collected at different discharge/charge states and corresponding discharge and charge curves under the current density of 0.2 A g^{-1}.

The ex situ X-ray diffraction (XRD) is performed to investigate the structural evolution and corresponding reaction mechanisms of the H-VO cathode upon selected charge and discharge states during the first two cycles. As displayed in Figure 2.10a, b, and c, the reflection pattern of the H-VO electrode at the initial state can match well with the as-synthesized $V_6O_{13}·nH_2O$, with the exclusion of the peak ascribed to the PTFE binder at 18°. When first discharged to 0.2 V at the current density of 0.2 A g^{-1}, the characteristic diffraction peak located at 7.8° representing the (001) plane with an interlayer spacing of 1.13 nm, shifts to a lower angle at 6.6° with a calculated d-spacing of 1.33 nm, and a series of new diffraction peaks appear at the 2θ angles of 13.1, 17.2, 19.6, and 30.6°, indicating a phase transition occurs. Notably, the interlamellar spacing expands from 1.13 nm to 1.33 nm upon in-depth discharge process, which is ascribed to the insertion of Zn^{2+} shielded by water molecules with reduced effective charge into the interlayer of the H-VO. Such favorable water shielding layer provides electrostatic shielding effect for Zn^{2+}, which can lower the activation energy for its ingress into the host structure, and thus contributing to effectively facilitating the fast Zn^{2+} diffusion. Furthermore, the peak intensity of the (001) facet

shows a dramatic increase, which manifests the change of crystallinity initiated by the intercalation of Zn^{2+} during the initial discharge process. At the following fully charged state, a slight contraction from 1.33 nm to 1.07 nm is observed due to the deintercalation of Zn^{2+}, and the new peaks initially formed during the previous first discharge process remain with slight shifts to 12.3, 16.9, 20.9, 30.1° respectively. As shown in Figure A8, these remained four new peaks can be well indexed to the pure phase of $Zn_3V_2O_7(OH)_2{\cdot}2H_2O$ (JCPDS no. 01-087-0417, space group: P-3m1), revealing an irreversible phase transition from $V_6O_{13}{\cdot}nH_2O$ to $Zn_xV_2O_7(OH)_2{\cdot}2H_2O$ ($x > 3$) during the previous discharge process, which is in accord with the irreversible reduction peak at 1.07 V from the first cathodic CV curve. It should be noted that the V-O-V pillars support the zinc oxide layers to form the layered $Zn_3V_2O_7(OH)_2{\cdot}2H_2O$ with porous crystal framework, which is advantageous for Zn^{2+} migration in its lattice. Subsequently, when secondly discharged to 0.8 V, the major peak of $V_6O_{13}{\cdot}nH_2O$ attributed to (001) plane repeatedly shifts to the same lower angle of 6.6°, while the peak of $Zn_3V_2O_7(OH)_2{\cdot}2H_2O$ at 12.3° slightly shifts to 13.1° with the corresponding lattice spacing only decreased by 6%. It is speculated that the expanded interlayer of $V_6O_{13}{\cdot}nH_2O$ is ascribed to the insertion of water-shielding Zn^{2+} with reduced effective charge as mentioned above, while the interlayer contraction of $Zn_3V_2O_7(OH)_2{\cdot}2H_2O$ is induced by the intense electrostatic interaction between bare Zn^{2+} and vanadium-oxygen layers, as supported by related reported $V_2O_5{\cdot}nH_2O$/graphene cathode,[28] and $Na_2V_6O_{16}{\cdot}1.63H_2O$ cathode[44] in aqueous ZIBs respectively. Reversibly, the fully charged electrode at 1.4 V at the second cycle, showed the same XRD pattern again as the electrode after the first cycle does, suggesting the reversible transformation between $Zn_aV_6O_{13}{\cdot}mH_2O/Zn_xV_2O_7(OH)_2{\cdot}2H_2O$ and $Zn_bV_6O_{13}{\cdot}mH_2O/Zn_yV_2O_7(OH)_2{\cdot}2H_2O$ ($a > b$, $x > y$) after the first cycle. As revealed by the ex

situ XRD, the electrochemical reaction is different between the first discharge process and subsequent discharge process. Notably, this difference can be observed from a small, irreversible reduction peak at 1.07 V in the initial cathodic CV curve. We speculate that this irreversible reduction peak is so small that the difference in the charge-discharge profiles may not be obviously observed. In addition, the structural change of H-VO after a series of cycles at fully charged states is further investigated. As displayed in Figure A9, the major peak of $V_6O_{13}{\cdot}nH_2O$ at 8.3° negatively shifts to 6.5°, while the major peak of $Zn_3V_2O_7(OH)_2{\bullet}2H_2O$ at 12.4° positively shifts to 13.1° after the first cycle, indicating a specific amount of water molecules and Zn^{2+} from electrolyte may be trapped in the crystal structure, which accounts for the structural change and gradual capacity decay. After 200 cycles, the XRD patterns of H-VO show no obvious difference, implying the good structure preservation with high durability, consistent with its desirable long-term cycling stability.

In consequence, the schematic illustration of Zn^{2+} storage mechanism is shown in Figure 2.11. The corresponding electrochemical mechanism of the Zn/H-VO rechargeable battery is displayed as follows:

Anode:

$Zn \longleftrightarrow Zn^{2+} + 2e^-$

Cathode:

$V_6O_{13}{\cdot}nH_2O + (a+x)Zn^{2+} + 2(a+x)e^- + (m-n+2)H_2O \longleftrightarrow Zn_aV_6O_{13}{\cdot}mH_2O +$

$Zn_xV_2O_7(OH)_2{\cdot}2H_2O$ (In the first discharge process)

$Zn_aV_6O_{13}{\cdot}mH_2O + Zn_xV_2O_7(OH)_2{\cdot}2H_2O \longleftrightarrow Zn_bV_6O_{13}{\cdot}mH_2O + Zn_yV_2O_7(OH)_2{\cdot}2H_2O +$

$(a+x-b-y)Zn^{2+} + 2(a+x-b-y)e^-$ (In the subsequent cycles)

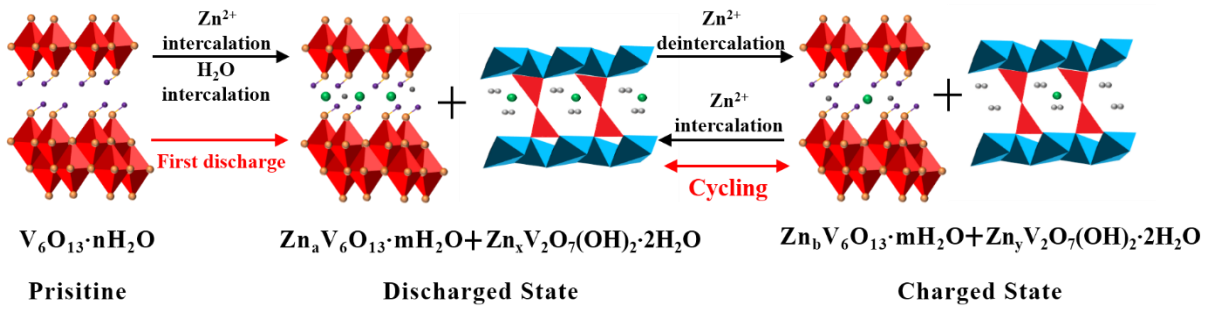

Figure 2.5. Schematic illustration of Zn^{2+} and water co-intercalation into H-VO electrode during the initial discharge process and reversible Zn^{2+} extraction/insertion in the subsequent process.

2.3. Conclusion

In summary, we design and develop a novel aqueous rechargeable ZIB based on the H-VO cathode with a high potential for large-scale and cost-effective production. Owing to numerous transportation channels offered by large interlamellar spacing (1.13 nm) and short diffusion pathways benefiting from the unique hollow microflower structure, the H-VO cathode delivers a high specific capacity of 395 mAh g^{-1} at 0.1 A g^{-1}, excellent rate capability with a considerable capacity of 97 mAh g^{-1} at an extremely high current density of 20 A g^{-1}, and excellent cycle durability with a high capacity retention of 87% up to 1000 cycles at 5 A g^{-1}. Our result demonstrates that the $V_6O_{13}·nH_2O$ with greatly enhanced electrochemical performances possesses high potential for large-scale practical ZIB application, and it may shed light on the water-initiated effective interlayer engineering strategy for the construction of high-performance promising cathode materials in zinc ion storage system.

3. Hydrated $NH_4V_3O_8$ Nanobelts Electrode for Superior Aqueous and Quasi-Solid-State Zinc Ion Batteries

3.1. Experimental Section

$NH_4V_3O_8 \cdot 1.9H_2O$ (AVO-1) was synthesized through a hydrothermal method. In a typical synthesis, 1 g commercial V_2O_5 power was added into 5 mL ammonium hydroxide (28-30%). Subsequently, 40 mL of 0.1 M oxalic acid was added into the above solution, and the mixed solution was stirred for 30 min at room temperature. Later, the pH of the solution was adjusted to 3 by dropwise adding the hydrochloric acid (36%). Then, the solution was transferred into a 100 mL Teflon-lined autoclave and kept at 190 °C for 5 h. Finally, the product, AVO-1 was collected, washed with deionized water and ethanol several times, and then dried at 60 °C overnight. $NH_4V_4O_{10} \cdot 1.6H_2O$ (AVO-2) was synthesized by the same procedure, except for adding 40 mL of 0.2 M oxalic acid.

The quasi-solid-state electrolyte was prepared by the following procedure: 1g gelatin power was mixed with 5 mL of 1 M $ZnSO_4$ aqueous solution and kept stirring at 75 °C for 3 h. Later, the mixed solution was poured on a silicon wafer at room temperature to achieve the gel, which serves as the gel electrolyte.

The XRD data were collected at a constant scanning rate of 2° min^{-2} on a Rigaku MiniFlex X-ray diffractometer with Cu Kα radiation (λ = 1.5405 Å). SEM imaging was carried out on a FEI Quanta 3D FEG field emission scanning electron microscopy (FESEM). TEM and HRTEM imaging was performed on a JEOL JEM-2010 microscope at 200 kV. XPS measurements were

This chapter is reproduced by permission of The Royal Society of Chemistry from J. Lai, H. Tang, X. Zhu, Y. Wang, Hydrated $NH_4V_3O_8$ Nanobelts Electrode for Superior Aqueous and Quasi-Solid-State Zinc Ion Batteries. *Journal of Materials Chemistry A*, 2019, DOI: 10.1039/C9TA07822C.

recorded by an AXIS165 spectrometer. Thermogravimetry (TG) data were collected using an SII STA7300 analyzer under the nitrogen atmosphere.

The working electrode was fabricated by rolling 60 wt% active material, 30 wt% conductive carbon (Super P), and 10 wt% polytetrafluoroethylene (PTFE) into thin film. For the aqueous batteries, Zinc foil, 3 M zinc trifluoromethanesulfonate ($Zn(CF_3SO_3)_2$) or $ZnSO_4$ aqueous solution, and glass fiber membrane were used as the anode, electrolyte, and separator, respectively, which were assembled in 2032 coin-type cells. For the quasi-solid-state batteries, flexible Zinc foil and gelatin/$ZnSO_4$ gel electrolyte were employed as anode and electrolyte, correspondingly. Galvanostatic charge-discharge experiments were carried out on an eight-channel battery analyzer (MTI corporation) with a voltage range of 0.2-1.4 V. Cyclic voltammetry measurements and Electrochemical Impedance Spectroscopy was conducted on an electrochemical workstation (CHI 6504C) with a frequency range from 100 kHz to 0.01 Hz. Galvanostatic intermittent titration technique (GITT) measurements were operated on a potentiostat (VMP3, Bio-Logic). Before the GITT measurement, the assembled cell was first discharged and charged at 100 mA g^{-1} for one cycle to obtain a stable state. Subsequently, the assembled cell was discharged or charged at 50 mA g^{-1} for 30 min, and then rested for 60 min to make the voltage reach the equilibrium. The procedure was repeatedly applied to the cell during the entire charge-discharge process until reaching to the cut-off voltage (0.2 / 1.4 V).

3.2. Results and Discussion

Various layered hydrated ammonium vanadates are prepared through a simple hydrothermal method by tuning the concentration of oxalic acid precursor. Details of the preparation method can be found in the Supplemental Information. As presented in Figure 3.1a and B1a, the crystal structures of the as-synthesized powders are examined by XRD. The XRD

pattern of AVO-1 is indexed well to monoclinic $(NH_4)_2V_6O_{16}\cdot 1.5H_2O$ (JCPDS no. 00-051-0376), while the XRD pattern of AVO-2 matches monoclinic $NH_4V_4O_{10}$ (JCPDS no. 00-026-0096). Previous studies show that the most intense peak from XRD patterns of $NH_4V_3O_8$ prepared by hydrothermal method would become much weaker as the pH of reaction decreases and even become weaker than other characteristic peaks when pH approaches to 2.[45-46] Therefore, the most intense peak of our AVO-1 may be weak compared with other peaks, since the pH of the hydrothermal reaction is 3. In this case, those peaks in the range of 25°-30° or 50°-52° from AVO-1 are relatively strong, as the strongest peak becomes weaker. In addition, the XRD pattern of AVO-1 is consistent with that of hydrated $NH_4V_3O_8$.[47] The accessible large interplanar spacing plays a crucial part in boosting the electrochemical properties of the cathode in ZIBs, which can provide more ion diffusion pathways, and promote rapid migration of the electrolyte ions through the electrode. Notably, the interlayer distance at (002) plane of AVO-1 and the interlamellar spacing at (001) facet of AVO-2 is 8.1 Å and 9.4 Å, respectively, calculated based on Bragg's equation, which are comparable to the previously reported $K_{0.5}V_2O_5\cdot 0.76H_2O$,[49] $Na_2V_6O_{16}\cdot 3H_2O$,[39] $Ca_{0.25}V_2O_5\cdot nH_2O$,[48] and Zinc Pyrovanadate,[38] *etc*. The crystal structure of $NH_4V_3O_8$ is constructed by distorted VO_6 octahedra and VO_5 square pyramids with NH_4^+ cations between the vanadium-oxide layers, forming a zigzag layered structure. The NH_4^+ ions as the interlayer stabilizer can mitigate the structural change upon Zn^{2+} ingress. Additionally, $NH_4V_4O_{10}$ is built up of VO_6 octahedrons encapsulating ammonium ions to construct a typical layered structure. Both SEM and TEM are employed to study their corresponding morphological characteristics. As displayed in Figure 3.2b-c, AVO-1 exhibits a 3D porous urchin-like architecture with a size of ~ 25 μm, and high-resolution SEM image confirms that the urchin-like structure is constructed by one-dimensional nanobelts with widths ranging from 83 to 180 nm, which have the tendency to

form bundles. TEM further validates the nanobelt morphology of AVO-1, in accord with the high-resolution SEM images (Figure 3.3d-e). Similarly, the AVO-2 also displays an urchin-like structure with a size around 22 μm, composed of nanobelts with widths of 55-135 nm (Figure B1b-e). The favorable porous urchin-like architectures of both AVO-1 and AVO-2 would be beneficial for shortening the Zn^{2+} diffusion pathway, facilitating kinetics of Zn^{2+} insertion/extraction, and may render excellent electrochemical performances. The crystalline water content is calculated via the thermogravimetric analysis that is conducted within the temperature range of 35-600 °C in N_2 atmosphere. As depicted in Figure 3.4f and Figure B1f, the lattice water content is estimated to be 1.9 per $NH_4V_3O_8$ unit and 1.6 for each $NH_4V_4O_{10}$ unit respectively, based on their corresponding weight loss.

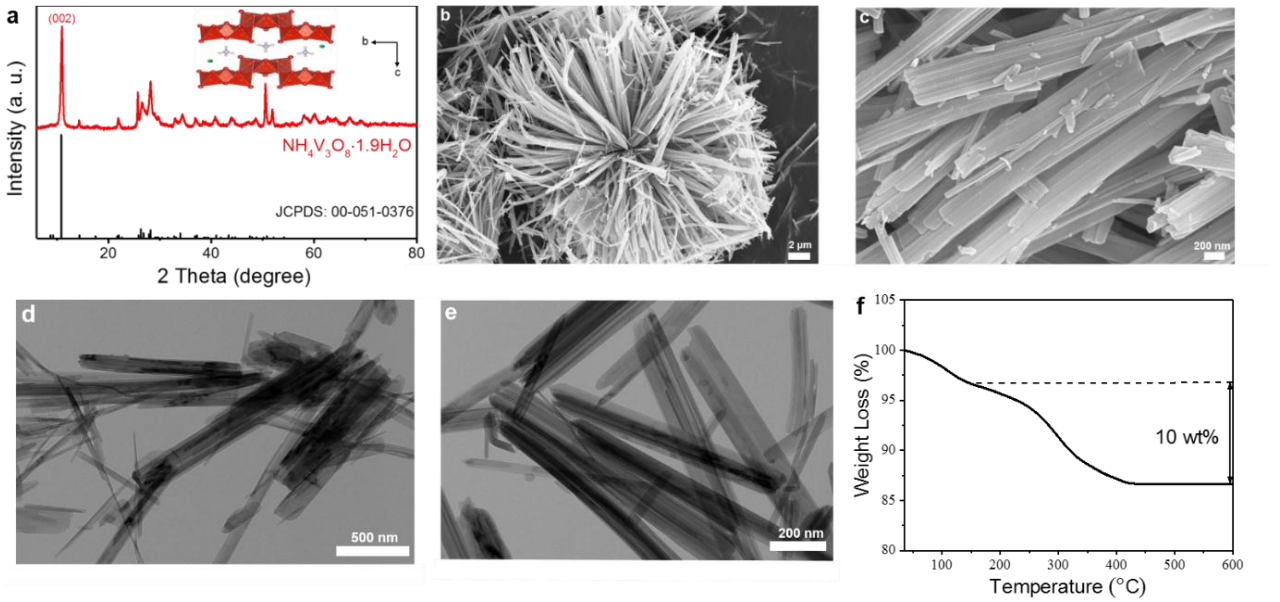

Figure 3.1. (a) Powder XRD pattern of as-synthesized AVO-1 and the inset displaying the crystal structure. (b-c) SEM images, (d-e) TEM images, and (f) Corresponding TGA result of AVO-1.

The electrochemical behaviors of AVO-1 and AVO-2 as ZIB cathodes are evaluated in the 2032 coin cells made in ambient atmosphere, by using 3 M $Zn(CF_3SO_3)_2$ aqueous electrolyte and metallic Zn foil anode. As displayed in Figure 3.5a, the first three cyclic voltammogram (CV)

curves of AVO-1 are recorded in a voltage range of 0.2-1.4 V (*vs.* Zn/Zn^{2+}) at 0.1 mV s^{-1}. Cathode peaks located at 0.78, 0.72, and 0.5 V are observed during the first reduction scan, which are slightly different from the peak positions at 0.8, 0.74, and 0.56 V in the following cycles of cathodic scan. The cathode peaks shifting can be attributed to the activation process of AVO-1 in the discharge state. Notably, a well-resolved cathodic peak at 0.72 V in the first CV cycle is observed, but it disappears in the next two cycles. This phenomenon occurs probably because the intercalated Zn^{2+} ions locate in the "dead Zn^{2+} sites", which is irreversible and cannot be extracted from the AVO-1 cathode during the subsequent anodic scan. Similar phenomenon can be observed in other aqueous ZIBs employing vanadate as cathode, such as in $Na_{0.33}V_2O_5$.[29] The initial three oxidation scans present entirely overlapping oxidation peaks located at 0.69 and 0.95 V. Several reduction and oxidation peaks are evidently observed, suggesting a multistep reaction process with respect to Zn^{2+} ingress/egress. Additionally, the CV profiles of initial three cycles exhibit good repeatability, except for the activation with slight peak shift in the first cathodic scan, indicating desirable reversibility and structural stability of the Zn/AVO-1 battery. Such CV curves are slightly different from those of $Na_2V_6O_{16}\cdot 3H_2O$[39] and zinc pyrovanadate[38] and thus its electrochemical behavior is slightly different, which may be ascribed to the variant cation pillars of NH_4^+ in AVO-1. Figure B3a shows the first three CV curves of the AVO-2 electrode, where the anodic peak at 0.76 V and the cathodic peak at 0.8 V are slightly different from the corresponding peaks of the following two cycles. Similar to the AVO-1 and other reported vanadates cathode used in aqueous ZIBs, the peak shift is ascribed to the activation process during the initial cycle.[27] Subsequently, a small peak at 0.9 V followed by two cathodic peaks at 0.83 and 0.57 V and two anodic peaks at 0.8 and 0.96 V can be observed. It should be noted that cathodic and anodic peaks of AVO-1 overlap more completely than those redox peaks of the AVO-2, except for the initial

CV cycle with activation process, indicating better electrochemical reversibility of the AVO-1 cathode.

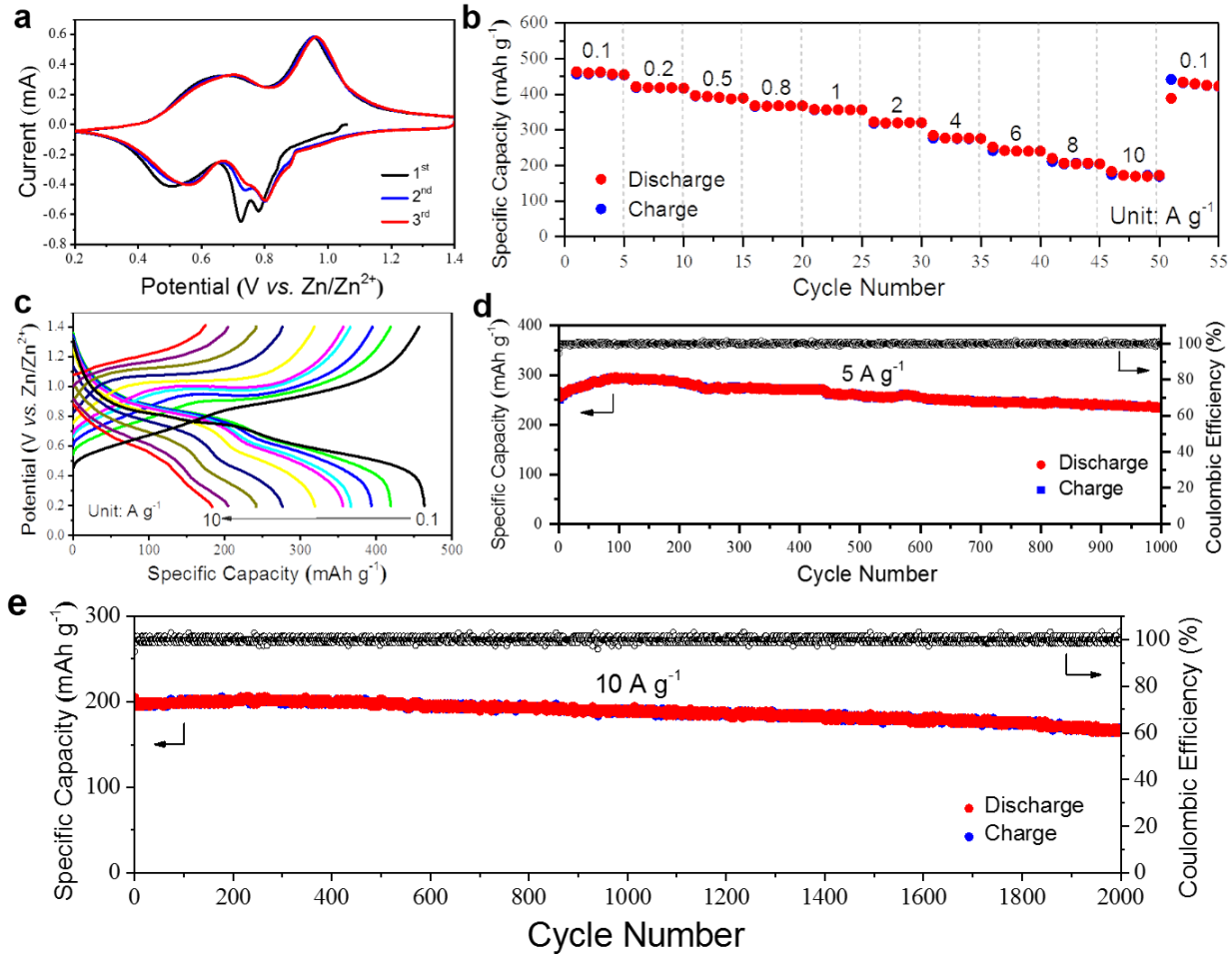

Figure 3.2. Electrochemical performances of the AVO-1 cathode in the potential range of 0.2-1.4 V *vs.* Zn/Zn^{2+}. (a) Initial three CV curves at 0.1 mV s^{-1}, (b) Rate property, (c) related discharge-charge profiles applied with different current densities, and (d-e) Long-term cycling performances at the current density of 5 and 10 A g^{-1}, respectively.

Employing the galvanostatic method with a specific current density of 0.1 A g^{-1}, the electrochemical profiles of AVO-1 upon Zn^{2+} ingress/egress are depicted in Figure B2. Remarkably, AVO-1 delivers a high initial discharge capacity of 463 mAh g^{-1} and charge capacity of 456 mAh g^{-1}, with a corresponding coulombic efficiency (CE) of 98.5%. This high initial CE suggests good reversibility of Zn^{2+} intercalation/deintercalation. The favorable first CE is mainly

attributed to the weakened electrostatic interactions between the host structure and Zn^{2+} with the assistance of crystalline water, and its stable layered framework pillared by NH_4^+. The discharge curves display two plateau-like parts in the voltage range of 0.9-0.65 and 0.65-0.4 V, while the charge curves present two plateau-like areas of 0.6-0.8 and 0.8-1.1 V, which correspond to the intercalation/deintercalation of Zn^{2+}. Notably, the charge-discharge profiles for the subsequent two cycles completely overlap, implying a good reversibility and structural stability of the AVO-1 electrode. Rate performance in aqueous ZIBs is one of the most important indicators to evaluate the electrochemical property and transport kinetics of Zn^{2+} during electrochemical reactions, which is essential to fulfill the increasing demands for grid-scale energy storage devices. Unfortunately, a variety of cathodes reported earlier present poor rate performances, due to the irreversible structure change and intensive polarization of Zn^{2+} with slow charge transfer kinetics.[21, 38, 49] However, the as-prepared AVO-1 electrode exhibits superior rate capability when subjected to harsh galvanostatic evaluation from 0.1 up to 10 A g^{-1} within a voltage window between 0.2 and 1.4 V, as illustrated in Figure 3.6b-c. The AVO-1 electrode exhibits reversible capacities of 463, 421, 396, 367, 357, 322, 284, 251, 220, and 183 mAh g^{-1} at a specific current of 0.1, 0.2, 0.5, 0.8, 1, 2, 4, 6, 8, 10 A g^{-1}, correspondingly. It should be noted that there is only ~38% capacity decay as the applied current density is amplified from 0.1 to 4 A g^{-1}. Furthermore, a decent average-capacity of 173 mAh g^{-1} is obtained even applied with the highest current rate of 10 A g^{-1}, and the associated discharge-charge time is ~62 s, suggesting the ultrafast transportation kinetics and impressive rate capability of the AVO-1 cathode. When the current rate abruptly recovers to 0.1 A g^{-1}, the discharge capacity is restored to 420 mAh g^{-1}, suggesting a strong tolerance ability for fast Zn^{2+} migration and high structural stability. The rate behavior of AVO-2 is elucidated with applied current density starting from 0.2 to 5 A g^{-1}, as presented in Figure B3b. Capacities of 384,

351, 324, 308, 257, 206, 162, and 123 mAh g^{-1} are recorded at 0.2, 0.5, 0.8, 1, 2, 3, 4, and 5 A g^{-1}, and the capacity can recover to 369 mAh g^{-1} when the current rate goes back to 0.2 A g^{-1}. Notably, the good rate performance of AVO-2 electrode is very competitive to the cathodes reported before.[38, 50-51] However, the rate capability of AVO-2 is much inferior compared with the AVO-1, suggesting the difference of Zn^{2+} diffusion kinetics in these two layered hydrated ammonium vanadates for aqueous ZIBs, which will be discussed later. The long cycling performances of AVO-1 and AVO-2 are further examined at a high specific current of 5 A g^{-1} under the galvanostatic test (Figure 3.7d and Figure B3c). The AVO-1 electrode provides a high initial capacity of 268 mAh g^{-1} with a CE over 94%, while AVO-2 presents a comparable discharge capacity of 288 mAh g^{-1} with a CE of 95%. Remarkably, a capacity retention over 87% is obtained for AVO-1, while only 65% capacity is retained for AVO-2 after 1000 cycles, demonstrating the superior cycling stability of AVO-1 than AVO-2. More significantly, an enduring and highly reversible capacity of 166 mAh g^{-1} over 2000 cycles at an exceptionally high specific current of 10 A g^{-1} is achieved with 81% retained capacity, further demonstrating the durable long-life cycling performance of the AVO-1 electrode (Figure 3.8e). In addition, 3M $ZnSO_4$ aqueous electrolyte is also employed to study the cycling property of AVO-1 at 5 A g^{-1}, showing lower reversible capacities and severe capacity loss when compared with those cells using 3M $Zn(CF_3SO_3)_2$ aqueous solution (Figure B4). This result is ascribed to rapider kinetics and higher reversibility of Zn plating/stripping in the batteries based on aqueous $Zn(CF_3SO_3)_2$ electrolyte than those with aqueous $ZnSO_4$ electrolyte, as bulky $CF_3SO_3^-$ ions are capable of passivating Zn anode, reducing the number of water molecules surrounding Zn^{2+}, and simultaneously mitigating the solvation effect.[61]

To investigate the fundamental mechanism behind the marked distinction of electrochemical properties between these two layered hydrated ammonium vanadates with very similar urchin-like morphology, the charge storage kinetics are quantified using CV method and galvanostatic intermittent titration technique (GITT). The representative CV profiles of the AVO-1 cathode under various sweep rates ranging from 0.1 to 1 mV s^{-1} are illustrated in Figure 3.9a. Notably, these CV profiles basically maintain similar shapes with the increasing scan rate, indicating excellent endurance for Zn^{2+} continuous ingress/egress. Based on the following equation: $i = av^b$, the b value can be confirmed in the range of 0.5-1.0, where the b value approaching 0.5 represents a diffusion-controlled process and the b value reaching 1.0 indicates a capacitive process. The above equation can be reorganized to $\log i = b \log v + \log a$. The linear relationships of log *i vs.* log *v* at the peak potentials are depicted in Figure 3.10b. The coefficients b of peaks 1, 2, 3 and 4 are determined to be 0.74, 0.73, 0.83, and 0.70 respectively, manifesting that the electrochemical reactions are controlled by both capacitive and diffusion-controlled processes. Moreover, the capacitive and diffusion-limited contributions can be quantitatively separated to a capacitive (k_1v) and a diffusion-controlled process ($k_2v^{1/2}$) from the current response (i) at a specific potential (V), based on the equation of i (V) = $k_1v + k_2v^{1/2}$. As presented in Figure 3.11c, ~53% of the current contribution is assigned to the capacitive property at 0.6 mV s^{-1}, accounting for the impressively high rate behavior of the AVO-1 electrode. As for AVO-2 cathode, the b values of the four peaks are 0.79, 0.53, 0.76, and 0.57 correspondingly, suggesting that the capacitive and diffusion-limited behaviors co-control the charge storage process (Figure B5a-b). 49% of the current is provided by the capacitive process at the same scan rate of 0.6 mV s^{-1} for AVO-2, which is lower than the capacitive contribution (over 53%) in AVO-1 (Figure B5c). The GITT is applied to explore the kinetics of Zn^{2+} migration during cycling by examining the Zn^{2+}

diffusion coefficient (D_{Zn}^{2+}). The D_{Zn}^{2+} can be determined by the following equation: $D_{Zn^{2+}} = \frac{4L^2}{\pi\tau}\left(\frac{\Delta E_s}{\Delta E_t}\right)^2$, where L is the Zn^{2+} diffusion length which is equal to the electrode thickness, τ is the time of applied current pulse, ΔE_s is the variation of steady-state potential for the related step, ΔE_t is the potential change of a one-step GITT test after eliminating the iR drop.[11, 52] As shown in Figure 3.12d-e and Figure B5d-e, the calculated Zn^{2+} diffusion coefficients of the AVO-1 electrode at each single-step GITT test during the overall discharge process are higher than the D_{Zn}^{2+} of AVO-2, suggesting faster Zn^{2+} diffusion in the AVO-1 electrode. The average value of D_{Zn}^{2+} is 1.18×10^{-8} cm^2 s^{-1} in AVO-1, which is ~2 times higher than 5.64×10^{-9} cm^2 s^{-1} in AVO-2 during the discharge process, supporting the better rate capability of AVO-1 than AVO-2.

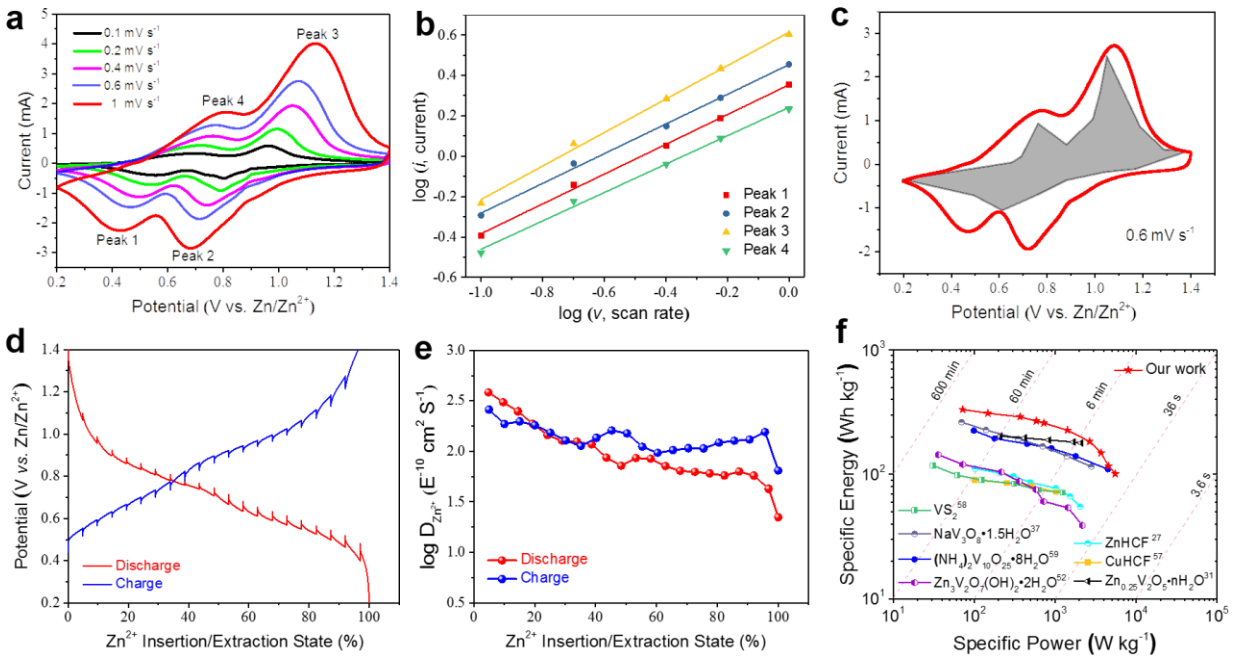

Figure 3.3. (a) CV profiles of the Zn/AVO-1 battery at a series of scan rates. (b) Log *i* versus log *v* plots at specific reduction/oxidation states based on the CV data. (c) CV curve showing the capacitive contribution (gray area) at 0.6 mV s^{-1}. (d) GITT profiles of the AVO-1 electrode. (e) Corresponding D_{Zn}^{2+} *vs* different Zn^{2+} (de)intercalation states. (f) The Ragone plots of the AVO-1 electrode and previously published cathodes for aqueous ZIBs.

The electrochemical impedance spectroscopy (EIS) tests are carried out to investigate the interfacial charge transfer process of AVO-1 and AVO-2, respectively (Figure B6). The charge-transfer resistance of AVO-1 (19.57 Ω) is lower than that of AVO-2 (22.41 Ω), which accounts for the better rate capability of AVO-1. Moreover, recent studies reveal that the lattice water can act as "lubricant" in layered vanadium-based compounds and plays a crucial role in enhancing their electrochemical performances for aqueous ZIBs.[28] The more crystalline water per unit of AVO-1 compared to AVO-2 may also contribute to the better electrochemical properties of AVO-1. In addition, structural change of AVO-1 during discharge and charge process in aqueous Zn/AVO-1 battery is investigated through ex situ XRD characterization. As presented in Figure B7, the XRD patterns of AVO-1 electrode at the pristine and charged states display similar patterns, while the (002) peak from the XRD patterns at the discharged state slightly shifts from 10.82° to 10.92°. Such slight peak shift indicates the negligible structural change of AVO-1 during Zn^{2+} intercalation, demonstrating structural stability and reversible Zn^{2+} insertion/extraction. Such phenomenon of negligible structural change can also be observed in layered $(NH_4)_2V_6O_{16}\cdot 1.5H_2O$ cathode for aqueous ZIBs, delivering ultra-stable cycling performance.[52] Notably, the well-preserved crystal structure of AVO-1 at the discharged state implies that the NH_4^+ would not be expelled during the first discharge process. To further explore the multistep oxidation-reduction reactions during Zn^{2+} ingress/egress, we obtain the XPS spectra of AVO-1 electrodes at pristine, fully discharged, and charged states. As shown in Figure B8a-b, there is no signal of Zn element in the pristine AVO-1, while two noticeable peaks related to Zn $2p_{3/2}$ and Zn $2p_{1/2}$ are detected at the fully discharged electrode, confirming the insertion of Zn^{2+} into the AVO-1 host. At the fully charged state, the corresponding peaks from Zn element become weaker but do not fully disappear, resulting from partially irreversible Zn^{2+} intercalation, which is consistent with the first CV curve

with partial irreversibility presented above (Figure B8c).[39] The valence states of V at different states are also investigated (Figure B8d-f). At the original state, V $2p_{3/2}$/V $2p_{1/2}$ peaks located at 517.54/525.23 eV are ascribed to the V $2p_{3/2}$ - V $2p_{1/2}$ spin-orbit doublet for V(V), while V $2p_{3/2}$/V $2p_{1/2}$ peaks at 516.17/524.02 eV are assigned to V(IV), which may result from the impurity of V_2O_5 precursor.[27, 52] At the discharged state, the characteristic binding energy of 517.71/525.29, 516.91/524.15, and 515.10/522.15 eV from V $2p_{3/2}$/V $2p_{1/2}$ peaks are attributed to V(V), V(IV), and V(III), correspondingly, revealing the reduction from V(V) to V(IV)/V(III) during Zn^{2+} insertion. When charged back to 1.4 V, most of V(IV)/V(III) is oxidized to V(V), demonstrating highly reversible Zn^{2+} insertion/extraction in AVO-1 lattice. Notably, the N element signal at three different states can be clearly observed, indicating that NH_4^+ would not be expelled during Zn^{2+} intercalation (Figure B8g-i).

The superior Zn^{2+} insertion/extraction performance of the AVO-1 electrode is further reflected by the Ragone plots in comparison with recently reported cathode materials (based on the active mass of cathodes) for aqueous ZIBs, including $(NH_4)_2V_{10}O_{25}\cdot 8H_2O$,[53] ZnHCF,[54] VS_2,[43] $NaV_3O_8\cdot 1.5H_2O$,[49] $Zn_{0.25}V_2O_5\cdot nH_2O$,[25] etc. As presented in Figure 3.13f, AVO-1 electrode achieves the highest energy density of 332 Wh kg^{-1} at a power density of 72 W kg^{-1}, and a decent energy density of 101 Wh kg^{-1} can be realized with an ultrahigh power density of 5519 W kg^{-1}, which outperforms the ZIB cathode materials published before,[25, 38, 43, 49, 53-55] demonstrating its huge potential for grid energy storage systems. It is worthwhile to mention that the integral Zn/AVO-1 aqueous battery exhibits considerable energy density of 209 Wh kg^{-1} at 45 W kg^{-1} (Calculated by the 200% Zn anode and the cathode), which surpasses various conventional aqueous batteries, including Pb-acid batteries (~35 Wh kg^{-1}) and aqueous Li-ion batteries (40-85 Wh kg^{-1}). Moreover, the Zn^{2+} storage properties of previously published vanadium-based

electrodes in ZIBs are listed in Table S1. Compared to the other cathodes, our AVO-1 electrode exhibits the highest reversible capacity of 463 mAh g^{-1} at 0.1 A g^{-1}, the considerable capacity of 268 mAh g^{-1} with 87% retained capacity for 1000 cycles at 5 A g^{-1}, and an impressive capacity of 166 mAh g^{-1} after 2000 cycles at 10 A g^{-1}.

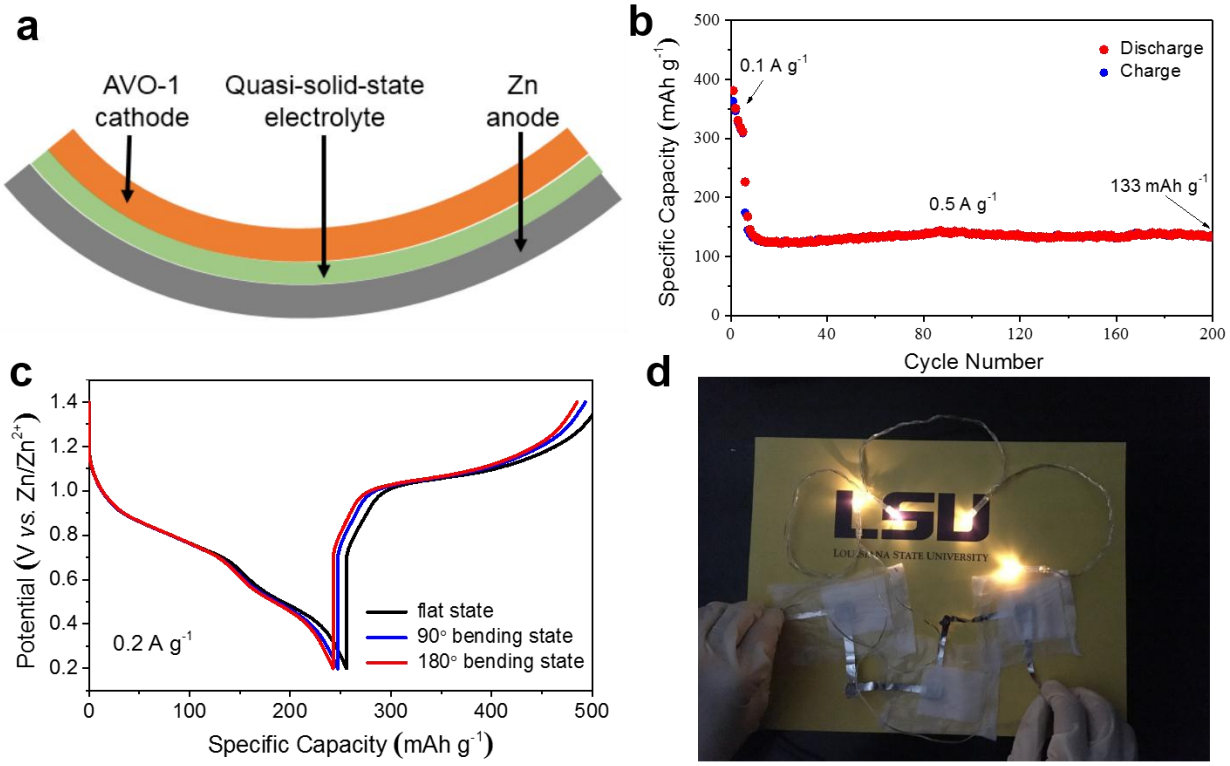

Figure 3.4. (a) Schematic illustration of the as-assembled flexible QSS Zn/AVO-1 cell by employing flexible Zn foil as anode, $ZnSO_4$/gelatin gel as QSS electrolyte, and AVO-1 nanobelts as cathode. (b) Long-term Cycling property with applied current density of 0.1 A g^{-1} for the initial five cycles and 0.5 A g^{-1} for the subsequent cycles. (c) Typical charge-discharge profiles under various bending states at 0.2 A g^{-1}. (d) A digital picture of four LED lights powered by three flexible QSS batteries in series.

Inspired by the superiority of the QSS ZIBs and the high electrochemical performances of the AVO-1 positive electrode in aqueous ZIBs, flexible Zn/AVO-1 battery were constructed by employing $ZnSO_4$/gelatin water-based QSS electrolyte, flexible Zn anode, and AVO-1 cathode (Figure 3.14a). The as-assembled QSS Zn/AVO-1 battery delivers high capacities of 378, 264, 203, 142, and 115 mAh g^{-1} at 0.1, 0.2, 0.5, 0.8, and 1A g^{-1}, correspondingly (Figure B9). Furthermore,

the reversible discharge capacity can retain 276 mAh g^{-1} as the current rate goes back from 1 to 0.1 A g^{-1}. Notably, the electrochemical properties of the QSS Zn/AVO-1 battery are not as good as those of the aqueous counterpart, owing to the lower ionic conductivity of the gel, but QSS ZIBs can still deliver competitive electrochemical performances. The long-term cycling property is evaluated with applied specific current of 0.1 A g^{-1} for the initial five cycles and 0.5 A g^{-1} for subsequent cycles. As shown in Figure 3.15b, the specific discharge capacity of 381 mAh g^{-1} is achieved, consistent with the rate behaviors at 0.1 A g^{-1}, and the discharge capacities stabilize at ~140 mAh g^{-1} at 0.5 A g^{-1} after five cycles with retained capacity of 133 mAh g^{-1} after 200 cycles, manifesting the good cycling performance of the as-assembled QSS battery. Furthermore, such long-term cyclability of Zn/AVO-1 cell is superior to that of the Zn/$V_5O_{12}\cdot 6H_2O$ QSS cell,[56] and comparable to the Zn/PANI cell.[57] As depicted in Figure B10a, the first discharge curve of the QSS Zn/AVO-1 battery presents two plateau-like areas in the voltage range of 0.95-0.73 and 0.65-0.45 V, while the following charge curve shows one plateau-like part of 0.9-1.1 V. The corresponding CV profile is relatively narrow compared to that of aqueous cells (Figure B10b). Furthermore, the EIS curves of QSS Zn/AVO-1 cell display a higher charge-transfer resistance compared with that of aqueous Zn/AVO-1 battery, suggested by a much wider semicircle that represents the enlarged charge-transfer resistance (788.6 Ω) (Figure B11). In addition, water from the QSS electrolyte can get involved in the electrochemical reactions, since it is one of the main compositions in the electrolyte. As displayed in Figure B12, the XRD pattern of the Zn anode at the first fully discharged state in QSS Zn/AVO-1 cell confirms the co-existence of Zn and $Zn_4(SO_4)(OH)_6\cdot 5H_2O$, which is consistent with previous reports on vanadium-based cathodes for aqueous or QSS ZIBs.[49,6358] To demonstrate the high potential for flexible energy storage devices, the galvanostatic behaviors of the QSS battery enduring different bending states are presented in

Figure 3.16c. The flexible Zn/AVO-1 battery exhibits specific discharge capacities of 255, 247, and 243 mAh g^{-1} at the flat state, 90° and 180° bending states with applied current of 0.2 A g^{-1}, showing negligible capacity loss under various bending states and maintaining similar discharge-charge profiles, demonstrating desirable flexibility. In addition, three QSS Zn/AVO-1 cells in series can successfully power up four LED lights (Figure 3.17d). As such, the results above show the QSS Zn/AVO-1 battery can serve as promising flexible energy storage devices.

3.3. Conclusion

In summary, layered hydrated ammonium vanadates including $NH_4V_3O_8 \cdot 1.9H_2O$ (AVO-1) and $NH_4V_4O_{10} \cdot 1.6H_2O$ (AVO-2) nanobelts are investigated as cathodes for rechargeable aqueous and QSS ZIBs. The charge storage kinetics of the AVO-1 and AVO-2 electrodes are evaluated by employing the CV method and the GITT. It is found that the AVO-1 exhibits larger capacitive contribution under the same scanning rate and higher D_{Zn}^{2+} than those of AVO-2. As expected, the AVO-1 cathode demonstrates better electrochemical performances regarding the rate behaviors and cycling property. Benefiting from the large interlayer spacing of 8.1 Å with easily accessible channels for Zn^{2+} diffusion, favorable nanoscale morphology, and stable NH_4^+ as interlayer "pillars", the as-prepared AVO-1 electrode exhibits large reversible capacity of 463 mAh g^{-1} at 0.1 A g^{-1}, high-rate capability up to 10 A g^{-1} with considerable discharge capacity of 183 mAh g^{-1}, and excellent long-cycle life (87% capacity retention after 1000 cycles at 5 A g^{-1} and 81% capacity retention over 2000 cycles at 10 A g^{-1} can be achieved). Furthermore, the investigated aqueous Zn/AVO-1 battery delivers competitive energy density of 209 Wh kg^{-1} at 45 W kg^{-1} (based on 200% Zn anode and the cathode). Additionally, a QSS flexible Zn/AVO-1 cell is constructed using gel electrolyte, where a decent capacity of 133 mAh g^{-1} is obtained for 200 cycles and the

electrochemical performance can be maintained under various bending states. Our result demonstrates that the $NH_4V_3O_8 \cdot 1.9H_2O$ electrode with impressive electrochemical properties in aqueous and QSS ZIBs holds high potential for grid-scale storage system and flexible energy storage devices.

4. Summary and Conclusion

In this report, rational design and synthesis of vanadium-based nanostructured materials (e.g., $V_6O_{13}{\cdot}nH_2O$ and $NH_4V_3O_8{\cdot}1.9H_2O$) has been developed to improve the electrochemical properties of cathode materials for rechargeable zinc ion batteries.

A simple hydrothermal method is employed to prepare the $V_6O_{13}{\cdot}nH_2O$ nanosheets. Featuring expanded interlayer spacing (1.13 nm) and unique hollow structure, the $V_6O_{13}{\cdot}nH_2O$ cathode shows a large capacity of 395 mAh g^{-1} at 0.1 A g^{-1}, superior rate capability with a capacity of 97 mAh g^{-1} at an extremely high current density of 20 A g^{-1}, and long-term cycling stability with a high capacity retention of 87% up to 1000 cycles at 5 A g^{-1}. The greatly improved electrochemical properties of $V_6O_{13}{\cdot}nH_2O$ compared to V_6O_{13} are ascribed to extended interlayer spacing with more accessible Zn^{2+} diffusion channels and lattice water as stable "pillars" preventing the structure collapse. By employing the GIIT measurement, the average D_{Zn}^{2+} of hydrated V_6O_{13} is 1.3 times higher than that of dehydrated V_6O_{13}, which convincingly support the much better rate capability of the $V_6O_{13}{\cdot}nH_2O$ electrodes than V_6O_{13}. The electrochemical reaction mechanism of $V_6O_{13}{\cdot}nH_2O$ cathodes in the integral aqueous batteries is investigated by a series of ex situ XRD characterization, based on the crystal structure changes at various discharged-charged states during Zn^{2+} intercalation/deintercalation. In addition, the crystal structures of $V_6O_{13}{\cdot}nH_2O$ electrodes after the 1^{st}, 200^{th}, 500^{th}, and 1000^{th} cycles are also examined by XRD characterization.

The hydrated ammonium vanadate, $NH_4V_3O_8{\cdot}1.9H_2O$ nanobelts is also studied as promising cathodes for ZIBs. By using CV measurement, GITT method, and EIS test, the charge storage kinetics can be quantified, which accounts for the superior electrochemical performances of $NH_4V_3O_8{\cdot}1.9H_2O$ electrodes. The larger capacitive contribution from CV and high D_{Zn}^{2+} from

GITT may account for the impressive electrochemical behaviors of $NH_4V_3O_8 \cdot 1.9H_2O$. Moreover, the effective "pillars" (e.g., NH_4^+, H_2O) contribute to the stable crystal structure of $NH_4V_3O_8 \cdot 1.9H_2O$ during Zn^{2+} intercalation/deintercalation. As such, $NH_4V_3O_8 \cdot 1.9H_2O$ electrode displays a high capacity of 463 mAh g^{-1} at 0.1 A g^{-1}, remarkable capability (maintaining 183 mAh g^{-1} even at an extremely high current density of 10 A g^{-1}), and durable long-cycling life (e.g., 81% capacity retention over 2000 cycles at 10 A g^{-1}). Impressively, the $NH_4V_3O_8 \cdot 1.9H_2O$ electrode materials can deliver a high energy density of 332 Wh kg^{-1} at a power density of 72 W kg^{-1} and maintain an energy density of 101 Wh kg^{-1} at a high power density of 5519 W kg^{-1}. Such high-performance aqueous ZIBs are emerging as promising candidates for grid-scale energy storage systems. In addition, a QSS is synthesized and QSS flexible Zn/ $NH_4V_3O_8 \cdot 1.9H_2O$ cell is investigated, presenting a considerable capacity of 133 mAh g^{-1} for 200 cycles and the desirable electrochemical property under different bending states. The three flexible QSS $Zn/NH_4V_3O_8 \cdot 1.9H_2O$ batteries in series can successfully power up four LED lights. The above results display that QSS $Zn/NH_4V_3O_8 \cdot 1.9H_2O$ batteries can be used in wearable energy storage devices with high safe, low cost, favorable electrochemical performances, and satisfactory flexibility.

In conclusion, this work provides different strategies including interlayer expansion and stable NH_4^+ as "pillars" to construct high-performance electrodes for zinc ion storage. The nanostructured morphologies of the designed vanadium-based materials also contribute to improving their electrochemical properties as desirable zinc ion hosts. In the future, more efforts are supposed to be put on the design and development of excellent QSS, which are capable of working in a wide temperature range from subzero to high temperature. The concentrated zinc-based electrolyte is one of the ideal electrolytes in combination with polymers for the synthesis of

anti-freezing QSS for flexible zinc ion storage under subzero temperature, as they contribute largely to the freezing resistance, ion conductivity, and mechanical-chemical properties. The systematic investigations of QSS operating in harsh environment can boost the practical applications of flexible ZIBs, which show high potential used in aerospace, airplanes, or ocean vehicles.

Appendix A. Supporting Figures for Chapter 2

Figure A1. Synthetic scheme of V_6O_{13}•nH_2O.

The proposed reaction mechanism:

$V_2O_5 + H_2C_2O_4 \rightarrow (VO_2)_2C_2O_4 + H_2O$

$(VO_2)_2C_2O_4 + 2H_2C_2O_4 \rightarrow 2VOC_2O_4 + 2CO_2$

$12VOC_2O_4 + H_2O_2 + 2nH_2O \rightarrow 2V_6O_{13}$•$nH_2O + 18CO_2 + 6C$

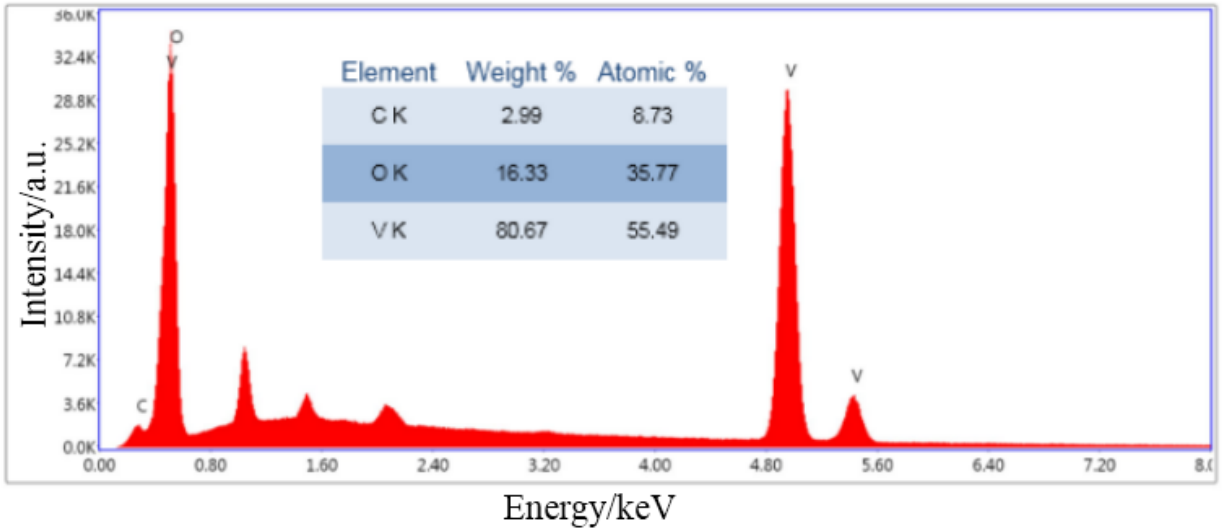

Figure A2. The EDS spectrum of as-synthesized H-VO material. The inset presents the corresponding elemental composition.

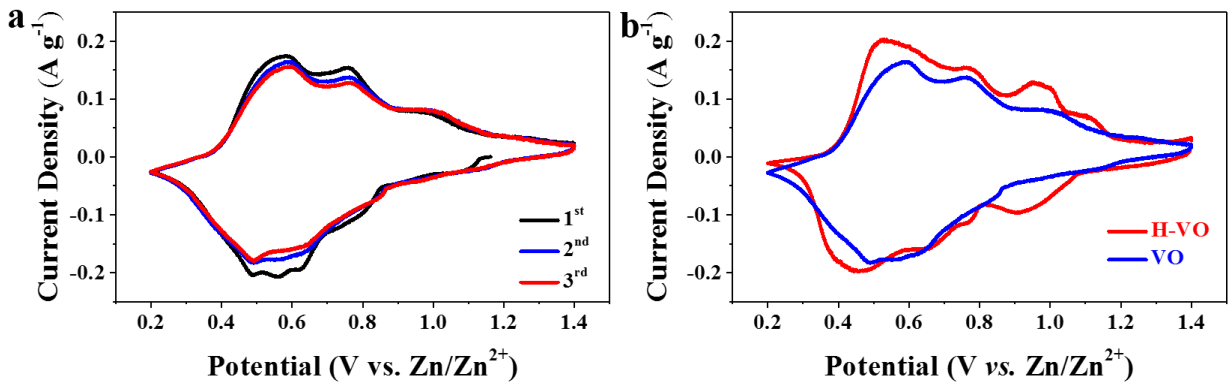

Figure A3. (a) Cyclic voltammograms of VO at 0.1 mV s^{-1} with the electrochemical voltage range of 0.2- 1.4 V vs. Zn/Zn^{2+}. (b) CV curves of H-VO and VO at a scan rate of 0.1 mV s^{-1} at the selected second cycle.

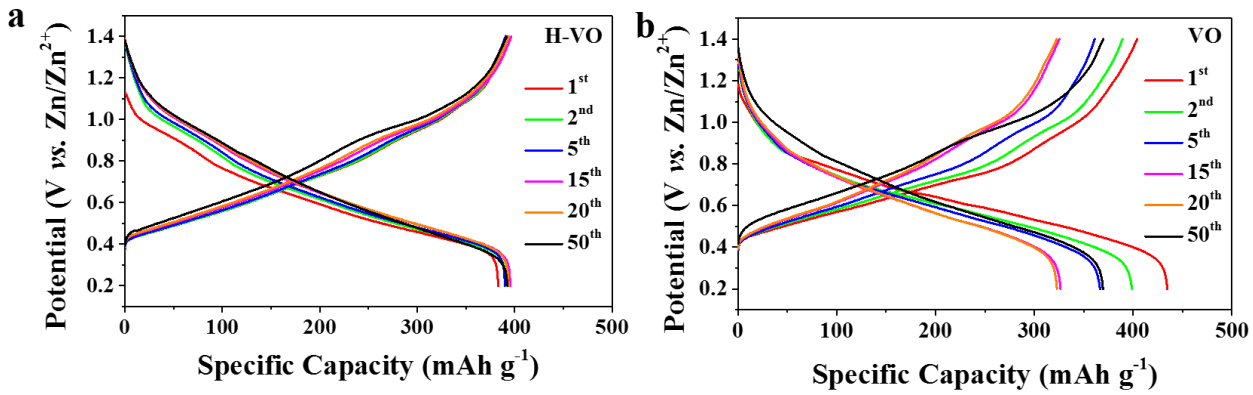

Figure A4. The galvanostatic discharge/charge curves of H-VO (a), and VO (b) at 0.1 A g^{-1}.

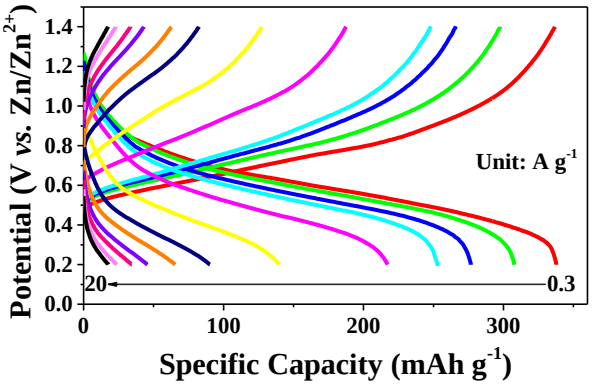

Figure A5. The galvanostatic discharge/charge profiles of VO applied with various current densities.

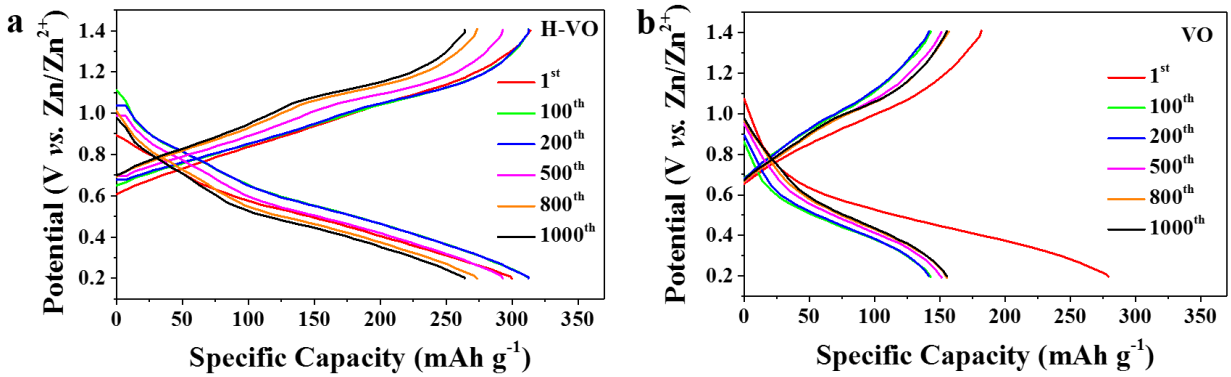

Figure A6. The galvanostatic discharge/charge curves of H-VO (a), and VO (b) at 5 A g^{-1}.

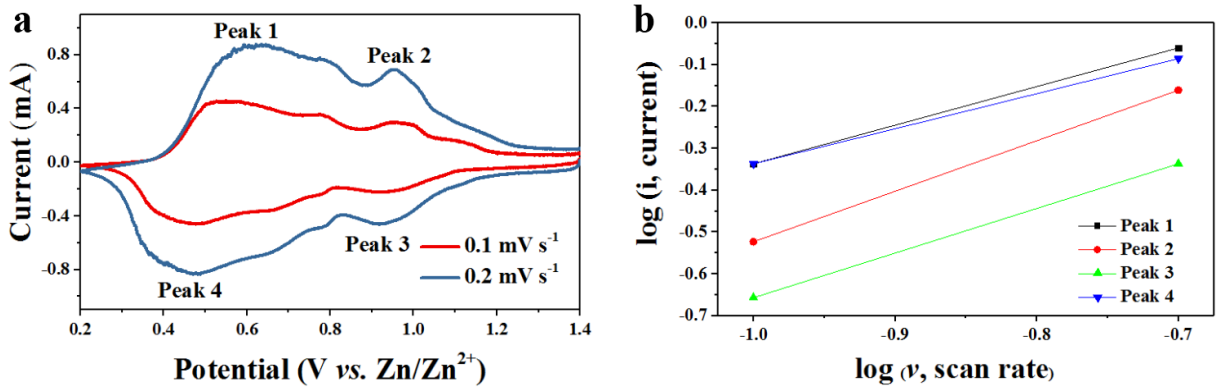

Figure A7. (a) CV profiles of the H-VO electrode at various scan rates. (b) log *i* versus log *v* plots from CV data at selected reduction/oxidation states.

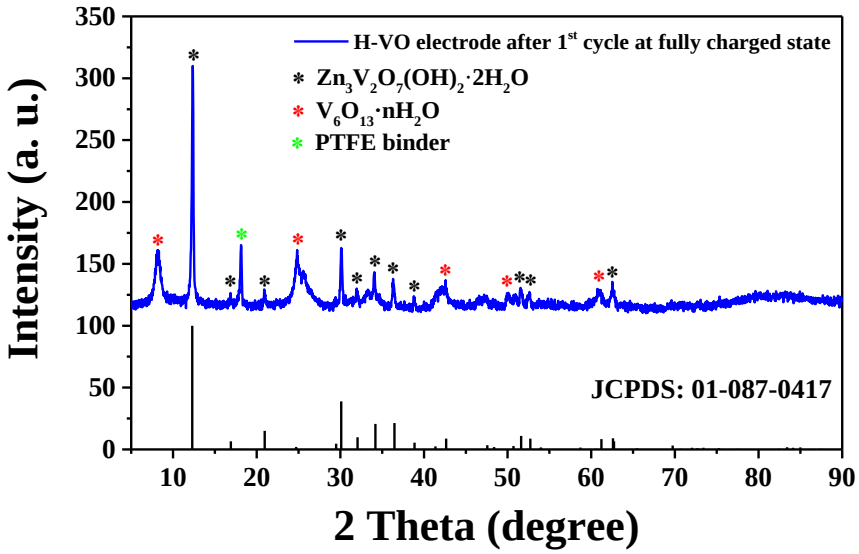

Figure A8. XRD patterns of the H-VO electrode after the first cycle at fully charged state and $Zn_3V_2O_7(OH)_2 \cdot 2H_2O$ (JCPDS no. 01-087-0417).

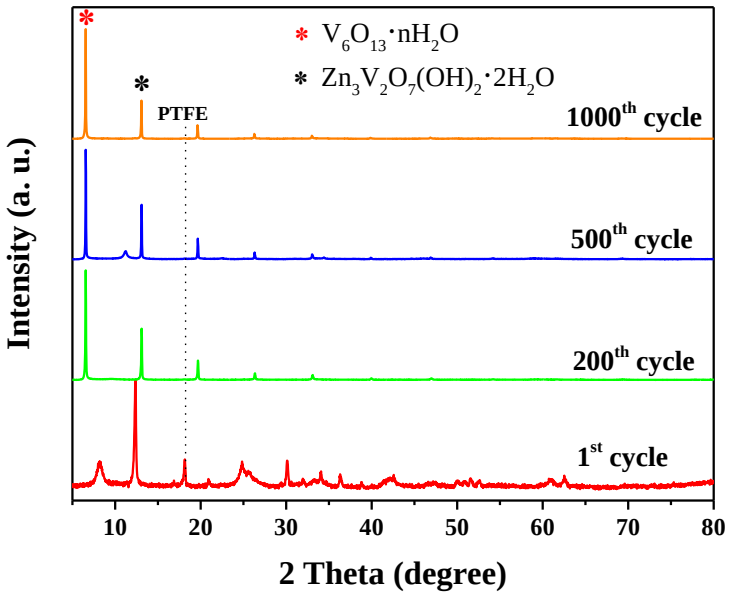

Figure A9. XRD patterns of H-VO electrode after various cycles at fully charged states.

Table A1. Comparison of our work with previous reported vanadium-based cathode materials on the electrochemical performances for aqueous zinc-ion battery

Electrode Material	Electrolyte	Specific capacity (mAh g^{-1})/ Current density (mA g^{-1})	Long-term cycling capacity (mAh g^{-1}) after x cycles at y mA g^{-1} with a capacity retention of z	Reference
$V_6O_{13}{\cdot}nH_2O$	3 M $Zn(CF_3SO_3)_2$	395/ 100	262 (x=1000, y=5000, z=87%)	Present work
$V_2O_5{\cdot}nH_2O$	3 M $Zn(CF_3SO_3)_2$ + 0.1 M vanadium sol	381/ 60	200 (x=900, y=6000, z=71%)	*Adv. Mater*. **2018**, 30, 1703725
VO_2 (B)	3 M $Zn(CF_3SO_3)_2$	357/ 100	250 (x=300, y=2000, z=91%)	*Adv. Mater*. **2018**, 1800762
$V_3O_7{\cdot}H_2O$	1 M $ZnSO_4$	375/ 375	216 (x=200, y=3000, z=80%)	*Energy Environ. Sci*. **2018**, 881-892
$VO_{1.52}(OH)_{0.77}$	1 M $ZnSO_4$	140/ 15	105 (x=50, y=15, z=70%)	*J. Mater. Chem. A.* **2017**, 8367-8375
VS_2	1 M $ZnSO_4$	190/ 50	111 (x=200, y=500, z=98%)	*Adv. Energy Mater*. **2017**, 7, 1601920
LiV_3O_8	1 M $ZnSO_4$	280/ 16	150 (x=65, y=133, z=75%)	*Chem. Mater*. **2017**, 29, 1684-1694
$Na_{0.33}V_2O_5$	3 M $Zn(CF_3SO_3)_2$	367/ 100	218 (x=1000, y=1000, z=93%)	*Adv. Energy Mater*. **2018**, 8, 1702463
$NaV_3O_8{\cdot}1.5H_2O$	1 M $ZnSO_4$ + 1 M Na_2SO_4	380/ 100	120 (x=1000, y=4000, z=82%)	*Nat. Commun.* **2018**, 9, 1656
$Na_2V_6O_{16}{\cdot}3H_2O$	1 M $ZnSO_4$	361/ 100	128 (x=1000, y=14440, z=80%)	*Nano lett.* **2018**, 18, 2402-2410
$Na_3V_2(PO_4)_3/C$	0.5 M $Zn(CH_3COO)_2$	97/ 50	72 (x=100, y=50, z=74%)	*Nano Energy*. **2016**, 211-217
$Zn_3V_2O_7(OH)_2{\cdot}2H_2O$	1 M $ZnSO_4$	213/ 50	101 (x=300, y=200, z=68%)	*Adv. Mater*. **2018**, 30, 1705580

Appendix B. Supporting Figures for Chapter 3

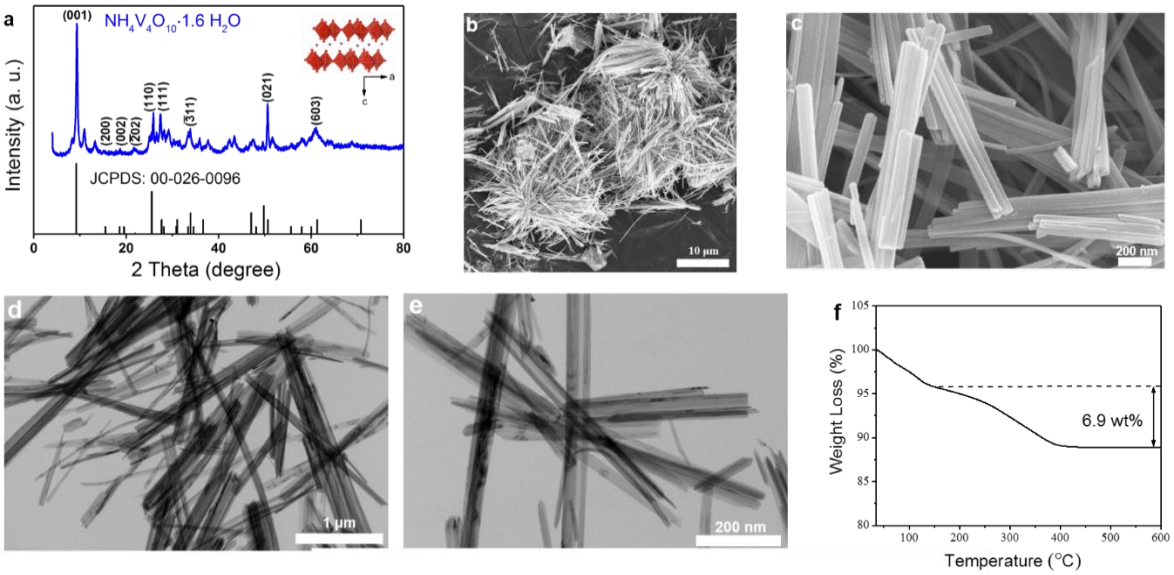

Figure B1. (a) XRD pattern and the inset showing the crystal structure, (b-c) SEM images, (d-e) TEM images, and (f) TGA result of the AVO-2.

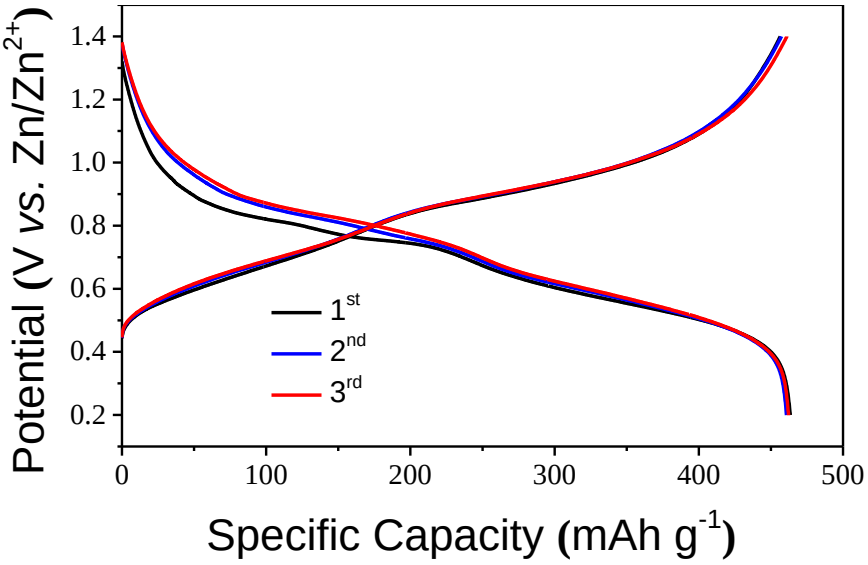

Figure B2. Discharge-charge profiles of the AVO-1 electrode at 0.1 A g^{-1}.

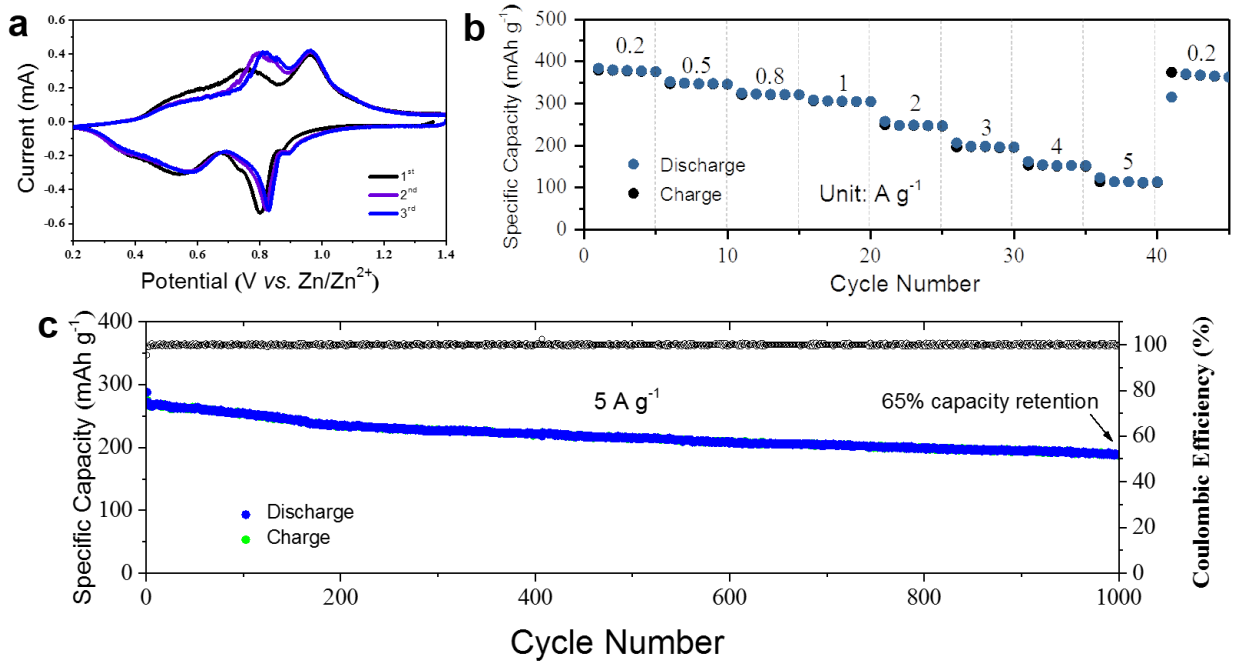

Figure B2. (a) CV curves at a scan rate of 0.1 mV s^{-1} in the initial three cycles, (b) rate performance, and (c) long-term cycling performance at the current density of 5 A g^{-1} of the AVO-2 electrode.

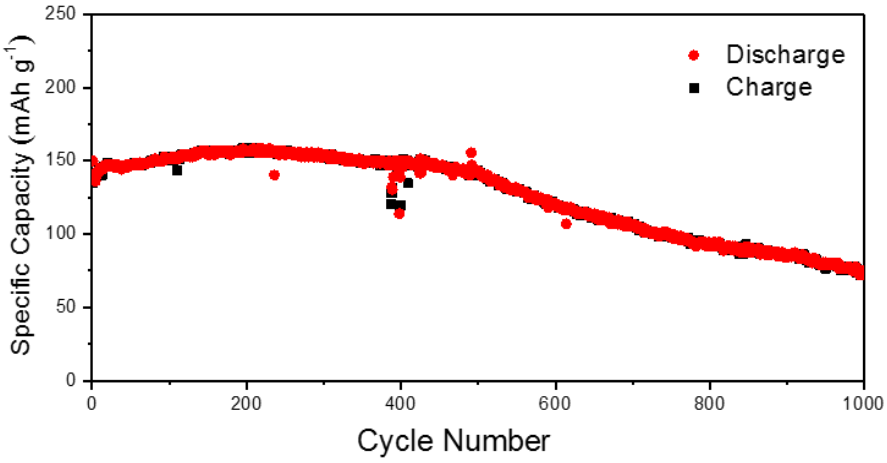

Figure B4. Cycling property of AVO-1 employing 3M $ZnSO_4$ aqueous electrolyte in the voltage range of 0.2-1.4 V at 5A g^{-1}.

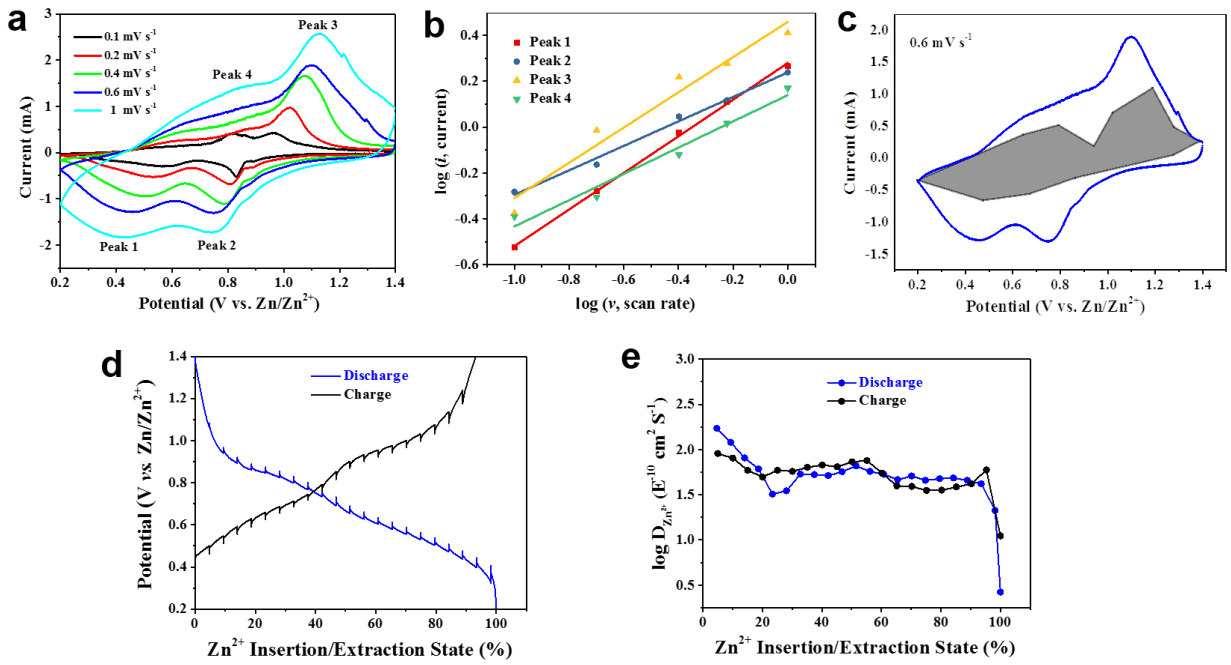

Figure B3. (a) CV profiles of the Zn/AVO-2 cell at different scan rates. (b) Log *i* versus log *v* plots at selected reduction/oxidation states based on the CV data. (c) CV curve showing the capacitive contribution (gray area) at 0.6 mV s^{-1}. (d) GITT curves of AVO-2 electrode. (e) Calculated diffusion coefficient of Zn^{2+} *vs.* various Zn^{2+} insertion/extraction states of AVO-2.

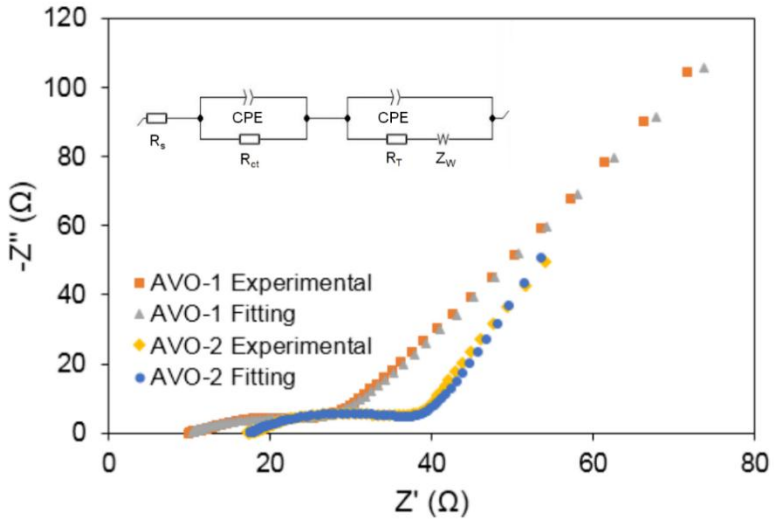

Figure B4. Electrochemical impedance spectroscopy curves of Zn/AVO-1 and Zn/AVO-2 aqueous batteries at the first charged state.

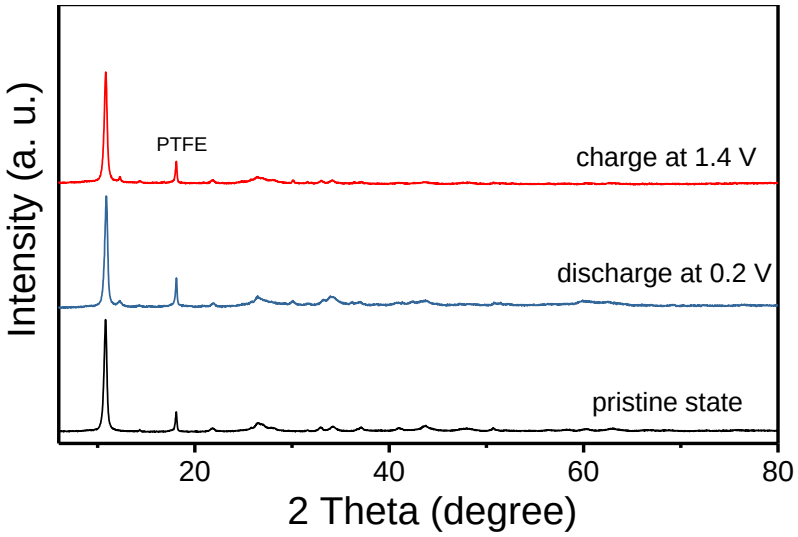

Figure B5. Ex situ XRD patterns of the AVO-1 cathode at various electrochemical states under the current density of 0.2 A g^{-1}.

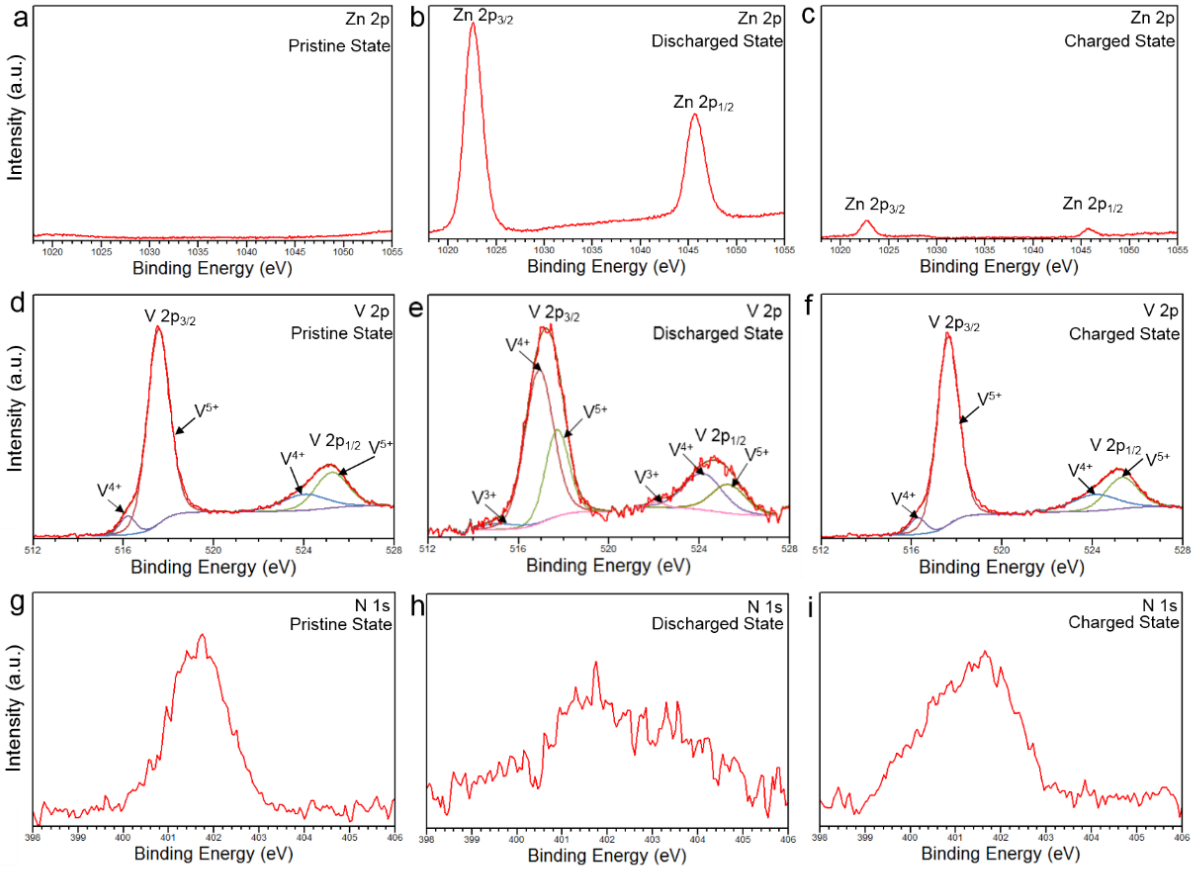

Figure B6. Ex situ XPS spectra of AVO-1 electrodes at various electrochemical states: (a-c) Zn 2p, (d-f) V 2p, (g-i) N 1s at the pristine, fully discharged, and fully charged states, respectively.

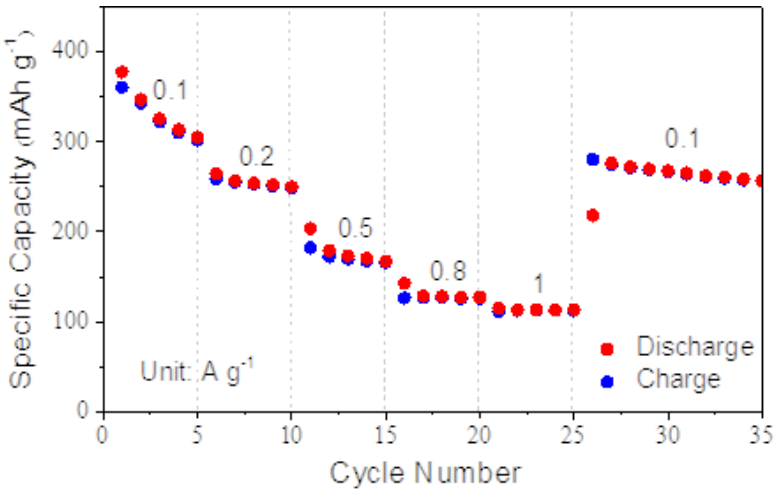

Figure B7. Rate capability of the QSS Zn/AVO-1 battery ranging from 0.1 A g^{-1} to 1 A g^{-1}.

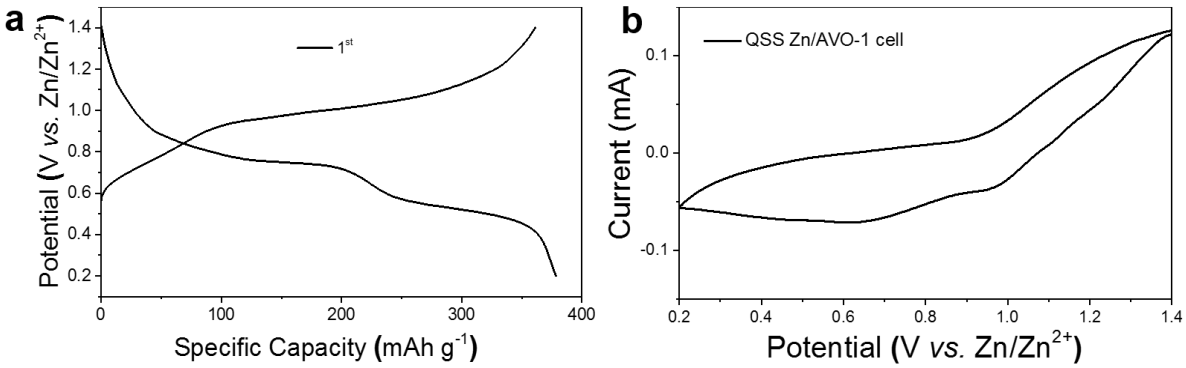

Figure B8. (a) Discharge-charge curves at 0.1 A g^{-1} and (b) CV profile at a scan rate of 0.5 mV s^{-1} of AVO-1 electrode in QSS batteries.

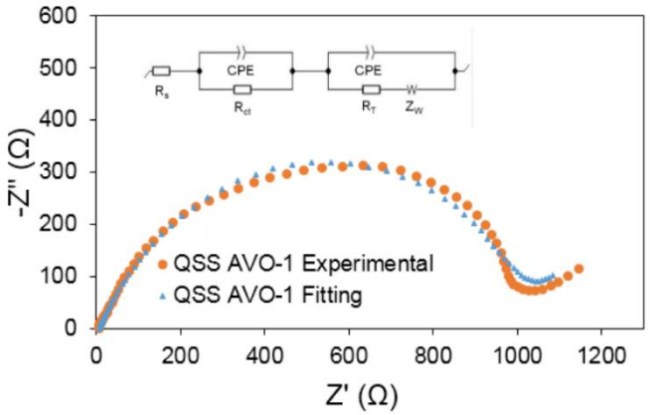

Figure B9. EIS curves of QSS Zn/AVO-1 battery at the first charged state.

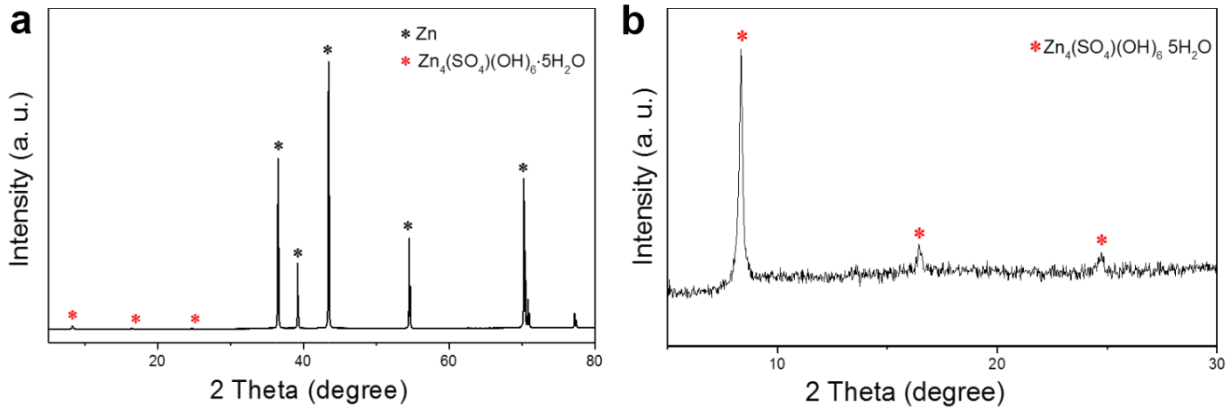

Figure B10. XRD pattern of Zn anode at the first fully discharged state in QSS Zn/AVO-1 cell with 2 theta of (a) 5-80°, (b) 5-30°.

Table B1. Comparison of our work with previous reported vanadium-based cathode materials on the electrochemical performances for aqueous zinc-ion battery.

Electrodes	Specific capacity (mAh g^{-1})/ Current density (mA g^{-1})	Long-term cycling capacity (mAh g^{-1}) after x cycles at y mA g^{-1} with a capacity retention of z	Reference
$NH_4V_3O_8 \cdot 1.9H_2O$	463/ 100	233 (x=1000, y=5000, z=87%) 166 (x=2000, y=10000, z=81%)	Present work
$V_2O_5 \cdot nH_2O$	381/ 60	200 (x=900, y=6000, z=71%)	*Adv. Mater*., 2018, **30**, 1703725
VO_2 (B)	357/ 100	250 (x=300, y=2000, z=91%)	*Adv. Mater*., 2018, **30**, 1800762
$V_3O_7 \cdot H_2O$	375/ 375	216 (x=200, y=3000, z=80%)	*Energy Environ. Sci*., 2018, **11**, 881-892
$VO_{1.52}(OH)_{0.77}$	140/ 15	105 (x=50, y=15, z=70%)	*J. Mater. Chem. A*, 2017, **5**, 8367-8375
VS_2	190/ 50	111 (x=200, y=500, z=98%)	*Adv. Energy Mater*., 2017, **7**, 1601920
LiV_3O_8	280/ 16	150 (x=65, y=133, z=75%)	*Chem. Mater*., 2017, **29**, 1684-1694
$Na_{1.1}V_3O_{7.9}$@rGO	238/ 50	171 (x=100, y=300, z=76%)	*Energy Storage Mater*., 2018, **13**, 168-174
$NaV_3O_8 \cdot 1.35H_2O$	366/ 100	200 (x=200, y=10000, z=100%)	*ACS Appl. Energy Mater*., 2018. **1**, 6401-6408
$Na_3V_2(PO_4)_3$/C	97/ 50	72 (x=100, y=50, z=74%)	*Nano Energy*, 2016, **25**, 211-217
$K_2V_8O_{21}$	247/ 300	208 (x=300, y=6000, z=83%)	*Nano Energy*, 2018, **51**, 579-587
$Zn_{0.25}V_2O_5 \cdot nH_2O$	300/ 50	208 (x=1000, y=2400, z=80%)	*Nat. Energy*., 2016, 1, 16119
$Zn_3V_2O_7(OH)_2 \cdot 2H_2O$	213/ 50	101 (x=300, y=200, z=68%)	*Adv. Mater*., 2018, **30**, 1705580

Appendix C. Copyright Information

Copyright Clearance Center RightsLink®

Home | Account Info | Help

ACS Publications
Most Trusted. Most Cited. Most Read.

Title: Interlayer-Expanded $V_6O_{13}{\cdot}nH_2O$ Architecture Constructed for an Advanced Rechargeable Aqueous Zinc-Ion Battery

Author: Jianwei Lai, Haihui Zhu, Xiuping Zhu, et al

Publication: ACS Applied Energy Materials

Publisher: American Chemical Society

Date: Mar 1, 2019

Copyright © 2019, American Chemical Society

Logged in as:
Jianwei Lai
Louisiana State University, Mechanical Engineering
Account #:
3001402882

LOGOUT

PERMISSION/LICENSE IS GRANTED FOR YOUR ORDER AT NO CHARGE

This type of permission/license, instead of the standard Terms & Conditions, is sent to you because no fee is being charged for your order. Please note the following:

- Permission is granted for your request in both print and electronic formats, and translations.
- If figures and/or tables were requested, they may be adapted or used in part.
- Please print this page for your records and send a copy of it to your publisher/graduate school.
- Appropriate credit for the requested material should be given as follows: "Reprinted (adapted) with permission from (COMPLETE REFERENCE CITATION). Copyright (YEAR) American Chemical Society." Insert appropriate information in place of the capitalized words.
- One-time permission is granted only for the use specified in your request. No additional uses are granted (such as derivative works or other editions). For any other uses, please submit a new request.

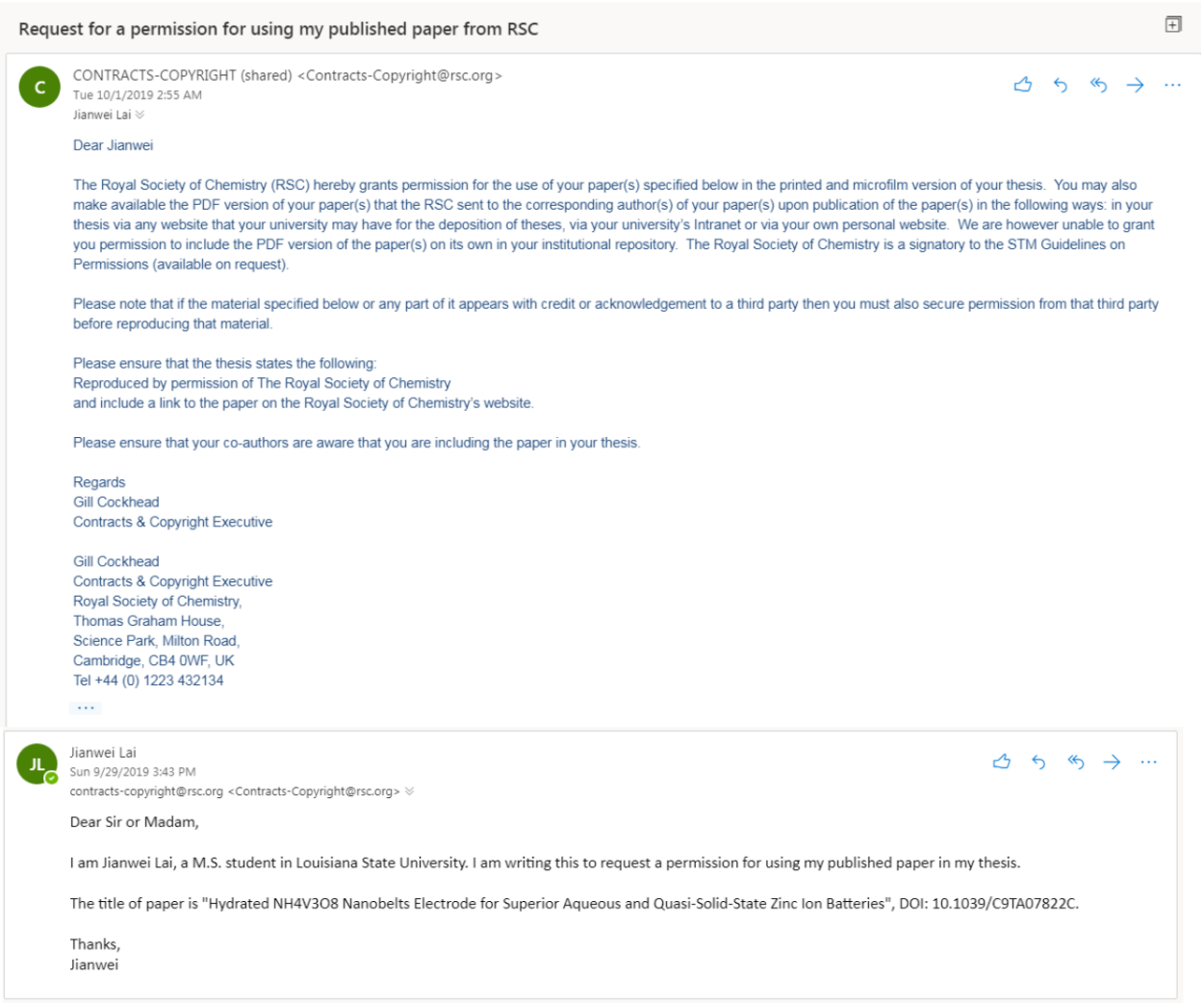

Request for a permission for using my published paper from RSC

CONTRACTS-COPYRIGHT (shared) <Contracts-Copyright@rsc.org>
Tue 10/1/2019 2:55 AM
Jianwei Lai

Dear Jianwei

The Royal Society of Chemistry (RSC) hereby grants permission for the use of your paper(s) specified below in the printed and microfilm version of your thesis. You may also make available the PDF version of your paper(s) that the RSC sent to the corresponding author(s) of your paper(s) upon publication of the paper(s) in the following ways: in your thesis via any website that your university may have for the deposition of theses, via your university's Intranet or via your own personal website. We are however unable to grant you permission to include the PDF version of the paper(s) on its own in your institutional repository. The Royal Society of Chemistry is a signatory to the STM Guidelines on Permissions (available on request).

Please note that if the material specified below or any part of it appears with credit or acknowledgement to a third party then you must also secure permission from that third party before reproducing that material.

Please ensure that the thesis states the following:
Reproduced by permission of The Royal Society of Chemistry
and include a link to the paper on the Royal Society of Chemistry's website.

Please ensure that your co-authors are aware that you are including the paper in your thesis.

Regards
Gill Cockhead
Contracts & Copyright Executive

Gill Cockhead
Contracts & Copyright Executive
Royal Society of Chemistry,
Thomas Graham House,
Science Park, Milton Road,
Cambridge, CB4 0WF, UK
Tel +44 (0) 1223 432134

Jianwei Lai
Sun 9/29/2019 3:43 PM
contracts-copyright@rsc.org <Contracts-Copyright@rsc.org>

Dear Sir or Madam,

I am Jianwei Lai, a M.S. student in Louisiana State University. I am writing this to request a permission for using my published paper in my thesis.

The title of paper is "Hydrated NH4V3O8 Nanobelts Electrode for Superior Aqueous and Quasi-Solid-State Zinc Ion Batteries", DOI: 10.1039/C9TA07822C.

Thanks,
Jianwei

Reproduced by permission of The Royal Society of Chemistry. The link of the paper entitled "Hydrated $NH_4V_3O_8$ Nanobelts Electrode for Superior Aqueous and Quasi-Solid-State Zinc Ion Batteries" is https://pubs.rsc.org/en/content/articlehtml/2019/ta/c9ta07822c.

References

(1) Goodenough, J. B.; Park, K.-S. The Li-ion rechargeable battery: a perspective. *Journal of the American Chemical Society* **2013,** *135* (4), 1167-1176.

(2) Yang, Z.; Zhang, J.; Kintner-Meyer, M. C.; Lu, X.; Choi, D.; Lemmon, J. P.; Liu, J. Electrochemical energy storage for green grid. *Chemical reviews* **2011,** *111* (5), 3577-3613.

(3) Whittingham, M. S. Lithium batteries and cathode materials. *Chemical reviews* **2004,** *104* (10), 4271-4302.

(4) Etacheri, V.; Marom, R.; Elazari, R.; Salitra, G.; Aurbach, D. Challenges in the development of advanced Li-ion batteries: a review. *Energy & Environmental Science* **2011,** *4* (9), 3243-3262.

(5) Tarascon, J.-M.; Armand, M. Issues and challenges facing rechargeable lithium batteries. In *Materials for Sustainable Energy: A Collection of Peer-Reviewed Research and Review Articles from Nature Publishing Group*; World Scientific: 2011; pp 171-179.

(6) Balakrishnan, P.; Ramesh, R.; Kumar, T. P. Safety mechanisms in lithium-ion batteries. *Journal of Power Sources* **2006,** *155* (2), 401-414.

(7) Song, M.; Tan, H.; Chao, D.; Fan, H. J. Recent Advances in Zn‐Ion Batteries. *Advanced Functional Materials* **2018,** *28* (41), 1802564.

(8) Fang, G.; Zhou, J.; Pan, A.; Liang, S. Recent advances in aqueous zinc-ion batteries. *ACS Energy Letters* **2018,** *3* (10), 2480-2501.

(9) Xu, C.; Li, B.; Du, H.; Kang, F. Energetic zinc ion chemistry: the rechargeable zinc ion battery. *Angewandte Chemie International Edition* **2012,** *51* (4), 933-935.

(10) Sun, W.; Wang, F.; Hou, S.; Yang, C.; Fan, X.; Ma, Z.; Gao, T.; Han, F.; Hu, R.; Zhu, M. Zn/MnO2 battery chemistry with H+ and Zn2+ coinsertion. *Journal of the American Chemical Society* **2017,** *139* (29), 9775-9778.

(11) Ding, J.; Du, Z.; Gu, L.; Li, B.; Wang, L.; Wang, S.; Gong, Y.; Yang, S. Ultrafast Zn2+ intercalation and deintercalation in vanadium dioxide. *Advanced Materials* **2018,** *30* (26), 1800762.

(12) Lee, S.-Y.; Choi, K.-H.; Choi, W.-S.; Kwon, Y. H.; Jung, H.-R.; Shin, H.-C.; Kim, J. Y. Progress in flexible energy storage and conversion systems, with a focus on cable-type lithium-ion batteries. *Energy & Environmental Science* **2013,** *6* (8), 2414-2423.

(13) Li, Q.; Zhang, Q.; Liu, C.; Zhou, Z.; Li, C.; He, B.; Man, P.; Wang, X.; Yao, Y. Anchoring V 2 O 5 nanosheets on hierarchical titanium nitride nanowire arrays to form core–shell heterostructures as a superior cathode for high-performance wearable aqueous rechargeable zinc-ion batteries. *Journal of Materials Chemistry A* **2019,** *7* (21), 12997-13006.

(14) Wang, Z.; Ruan, Z.; Liu, Z.; Wang, Y.; Tang, Z.; Li, H.; Zhu, M.; Hung, T. F.; Liu, J.; Shi, Z. A flexible rechargeable zinc-ion wire-shaped battery with shape memory function. *Journal of Materials Chemistry A* **2018,** *6* (18), 8549-8557.

(15) Zhang, S.; Yu, N.; Zeng, S.; Zhou, S.; Chen, M.; Di, J.; Li, Q. An adaptive and stable bio-electrolyte for rechargeable Zn-ion batteries. *Journal of Materials Chemistry A* **2018,** *6* (26), 12237-12243.

(16) Chao, D.; Zhu, C.; Song, M.; Liang, P.; Zhang, X.; Tiep, N. H.; Zhao, H.; Wang, J.; Wang, R.; Zhang, H. A High‐Rate and Stable Quasi‐Solid‐State Zinc‐Ion Battery with Novel 2D Layered Zinc Orthovanadate Array. *Advanced Materials* **2018,** *30* (32), 1803181.

(17) Huang, Y.; Liu, J.; Wang, J.; Hu, M.; Mo, F.; Liang, G.; Zhi, C. An Intrinsically Self‐Healing NiCo‖ Zn Rechargeable Battery with a Self‐Healable Ferric‐Ion‐Crosslinking Sodium Polyacrylate Hydrogel Electrolyte. *Angewandte Chemie International Edition* **2018,** *57* (31), 9810-9813.

(18) Mo, F.; Liang, G.; Meng, Q.; Liu, Z.; Li, H.; Fan, J.; Zhi, C. A flexible rechargeable aqueous zinc manganese-dioxide battery working at− 20° C. *Energy & Environmental Science* **2019,** *12* (2), 706-715.

(19) Lee, B.; Lee, H. R.; Kim, H.; Chung, K. Y.; Cho, B. W.; Oh, S. H. Elucidating the intercalation mechanism of zinc ions into α-MnO 2 for rechargeable zinc batteries. *Chemical Communications* **2015,** *51* (45), 9265-9268.

(20) Zhang, N.; Cheng, F.; Liu, J.; Wang, L.; Long, X.; Liu, X.; Li, F.; Chen, J. Rechargeable aqueous zinc-manganese dioxide batteries with high energy and power densities. *Nature communications* **2017,** *8* (1), 405.

(21) Alfaruqi, M. H.; Mathew, V.; Gim, J.; Kim, S.; Song, J.; Baboo, J. P.; Choi, S. H.; Kim, J. Electrochemically induced structural transformation in a γ-MnO2 cathode of a high capacity zinc-ion battery system. *Chemistry of Materials* **2015,** *27* (10), 3609-3620.

(22) Alfaruqi, M. H.; Gim, J.; Kim, S.; Song, J.; Pham, D. T.; Jo, J.; Xiu, Z.; Mathew, V.; Kim, J. A layered δ-MnO2 nanoflake cathode with high zinc-storage capacities for eco-friendly battery applications. *Electrochemistry Communications* **2015,** *60*, 121-125.

(23) Pan, H.; Shao, Y.; Yan, P.; Cheng, Y.; Han, K. S.; Nie, Z.; Wang, C.; Yang, J.; Li, X.; Bhattacharya, P. Reversible aqueous zinc/manganese oxide energy storage from conversion reactions. *Nature Energy* **2016,** *1* (5), 16039.

(24) Liu, Z.; Pulletikurthi, G.; Endres, F. A prussian blue/zinc secondary battery with a bio-ionic liquid–water mixture as electrolyte. *ACS applied materials & interfaces* **2016,** *8* (19), 12158-12164.

(25) Kundu, D.; Adams, B. D.; Duffort, V.; Vajargah, S. H.; Nazar, L. F. A high-capacity and long-life aqueous rechargeable zinc battery using a metal oxide intercalation cathode. *Nature Energy* **2016,** *1* (10), 16119.

(26) Tang, H.; Peng, Z.; Wu, L.; Xiong, F.; Pei, C.; An, Q.; Mai, L. Vanadium-based cathode materials for rechargeable multivalent batteries: challenges and opportunities. *Electrochemical Energy Reviews* **2018,** *1* (2), 169-199.

(27) Xie, Z.; Lai, J.; Zhu, X.; Wang, Y. Green Synthesis of Vanadate Nanobelts at Room Temperature for Superior Aqueous Rechargeable Zinc-Ion Batteries. *ACS Applied Energy Materials* **2018,** *1* (11), 6401-6408.

(28) Yan, M.; He, P.; Chen, Y.; Wang, S.; Wei, Q.; Zhao, K.; Xu, X.; An, Q.; Shuang, Y.; Shao, Y. Water‐lubricated intercalation in V2O5 • nH2O for high‐capacity and high‐rate aqueous rechargeable zinc batteries. *Advanced materials* **2018,** *30* (1), 1703725.

(29) He, P.; Zhang, G.; Liao, X.; Yan, M.; Xu, X.; An, Q.; Liu, J.; Mai, L. Sodium Ion Stabilized Vanadium Oxide Nanowire Cathode for High‐Performance Zinc‐Ion Batteries. *Advanced Energy Materials* **2018,** *8* (10), 1702463.

(30) Alfaruqi, M. H.; Mathew, V.; Song, J.; Kim, S.; Islam, S.; Pham, D. T.; Jo, J.; Kim, S.; Baboo, J. P.; Xiu, Z. Electrochemical zinc intercalation in lithium vanadium oxide: a high-capacity zinc-ion battery cathode. *Chemistry of Materials* **2017,** *29* (4), 1684-1694.

(31) Guo, X.; Fang, G.; Zhang, W.; Zhou, J.; Shan, L.; Wang, L.; Wang, C.; Lin, T.; Tang, Y.; Liang, S. Mechanistic insights of Zn2+ storage in sodium vanadates. *Advanced Energy Materials* **2018,** *8* (27), 1801819.

(32) Tang, B.; Zhou, J.; Fang, G.; Liu, F.; Zhu, C.; Wang, C.; Pan, A.; Liang, S. Engineering the interplanar spacing of ammonium vanadates as a high-performance aqueous zinc-ion battery cathode. *Journal of Materials Chemistry A* **2019,** *7* (3), 940-945.

(33) Ma, L.; Li, N.; Long, C.; Dong, B.; Fang, D.; Liu, Z.; Zhao, Y.; Li, X.; Fan, J.; Chen, S. Achieving Both High Voltage and High Capacity in Aqueous Zinc‐Ion Battery for Record High Energy Density. *Advanced Functional Materials* **2019**, 1906142.

(34) Ding, Y.-L.; Wen, Y.; Wu, C.; van Aken, P. A.; Maier, J.; Yu, Y. 3D V6O13 nanotextiles assembled from interconnected nanogrooves as cathode materials for high-energy lithium ion batteries. *Nano letters* **2015,** *15* (2), 1388-1394.

(35) Fei, H.; Lin, Y.; Wei, M. Facile synthesis of V6O13 micro-flowers for Li-ion and Na-ion battery cathodes with good cycling performance. *Journal of colloid and interface science* **2014,** *425*, 1-4.

(36) Xu, N.; Ma, X.; Wang, M.; Qian, T.; Liang, J.; Yang, W.; Wang, Y.; Hu, J.; Yan, C. Stationary full li-ion batteries with interlayer-expanded V6O13 cathodes and lithiated graphite anodes. *Electrochimica Acta* **2016,** *203*, 171-177.

(37) Wang, H.; Ren, Y.; Wang, W.; Huang, X.; Huang, K.; Wang, Y.; Liu, S. NH4V3O8 nanorod as a high performance cathode material for rechargeable Li-ion batteries. *Journal of Power Sources* **2012,** *199*, 315-321.

(38) Xia, C.; Guo, J.; Lei, Y.; Liang, H.; Zhao, C.; Alshareef, H. N. Rechargeable Aqueous Zinc‐Ion Battery Based on Porous Framework Zinc Pyrovanadate Intercalation Cathode. *Advanced Materials* **2018,** *30* (5), 1705580.

(39) Soundharrajan, V.; Sambandam, B.; Kim, S.; Alfaruqi, M. H.; Putro, D. Y.; Jo, J.; Kim, S.; Mathew, V.; Sun, Y.-K.; Kim, J. Na2V6O16· 3H2O barnesite nanorod: an open door to display a stable and high energy for aqueous rechargeable Zn-ion batteries as cathodes. *Nano letters* **2018,** *18* (4), 2402-2410.

(40) Sambandam, B.; Soundharrajan, V.; Kim, S.; Alfaruqi, M. H.; Jo, J.; Kim, S.; Mathew, V.; Sun, Y.-k.; Kim, J. Aqueous rechargeable Zn-ion batteries: an imperishable and high-energy Zn 2 V 2 O 7 nanowire cathode through intercalation regulation. *Journal of Materials Chemistry A* **2018,** *6* (9), 3850-3856.

(41) He, P.; Quan, Y.; Xu, X.; Yan, M.; Yang, W.; An, Q.; He, L.; Mai, L. High‐Performance Aqueous Zinc–Ion Battery Based on Layered H2V3O8 Nanowire Cathode. *Small* **2017,** *13* (47), 1702551.

(42) Deiss, E. Spurious chemical diffusion coefficients of Li+ in electrode materials evaluated with GITT. *Electrochimica Acta* **2005,** *50* (14), 2927-2932.

(43) He, P.; Yan, M.; Zhang, G.; Sun, R.; Chen, L.; An, Q.; Mai, L. Layered VS2 Nanosheet‐Based Aqueous Zn Ion Battery Cathode. *Advanced Energy Materials* **2017,** *7* (11), 1601920.

(44) Hu, P.; Zhu, T.; Wang, X.; Wei, X.; Yan, M.; Li, J.; Luo, W.; Yang, W.; Zhang, W.; Zhou, L. Highly durable Na2V6O16· 1.63 H2O nanowire cathode for aqueous zinc-ion battery. *Nano letters* **2018,** *18* (3), 1758-1763.

(45) Vernardou, D.; Apostolopoulou, M.; Louloudakis, D.; Katsarakis, N.; Koudoumas, E. Hydrothermal growth and characterization of shape-controlled NH 4 V 3 O 8. *New Journal of Chemistry* **2014,** *38* (5), 2098-2104.

(46) Zakharova, G.; Täschner, C.; Kolb, T.; Jähne, C.; Leonhardt, A.; Büchner, B.; Klingeler, R. Morphology controlled NH 4 V 3 O 8 microcrystals by hydrothermal synthesis. *Dalton Transactions* **2013,** *42* (14), 4897-4902.

(47) Mai, L.; Lao, C.; Hu, B.; Zhou, J.; Qi, Y.; Chen, W.; Gu, E.; Wang, Z. Synthesis and electrical transport of single-crystal NH4V3O8 nanobelts. *The Journal of Physical Chemistry B* **2006,** *110* (37), 18138-18141.

(48) Xia, C.; Guo, J.; Li, P.; Zhang, X.; Alshareef, H. N. Highly Stable Aqueous Zinc‐Ion Storage Using a Layered Calcium Vanadium Oxide Bronze Cathode. *Angewandte Chemie International Edition* **2018,** *57* (15), 3943-3948.

(49) Wan, F.; Zhang, L.; Dai, X.; Wang, X.; Niu, Z.; Chen, J. Aqueous rechargeable zinc/sodium vanadate batteries with enhanced performance from simultaneous insertion of dual carriers. *Nature communications* **2018,** *9* (1), 1656.

(50) Cai, Y.; Liu, F.; Luo, Z.; Fang, G.; Zhou, J.; Pan, A.; Liang, S. Pilotaxitic Na1. 1V3O7. 9 nanoribbons/graphene as high-performance sodium ion battery and aqueous zinc ion battery cathode. *Energy Storage Materials* **2018,** *13*, 168-174.

(51) Tang, B.; Fang, G.; Zhou, J.; Wang, L.; Lei, Y.; Wang, C.; Lin, T.; Tang, Y.; Liang, S. Potassium vanadates with stable structure and fast ion diffusion channel as cathode for rechargeable aqueous zinc-ion batteries. *Nano Energy* **2018,** *51*, 579-587.

(52) Wang, X.; Xi, B.; Feng, Z.; Chen, W.; Li, H.; Jia, Y.; Feng, J.; Qian, Y.; Xiong, S. Layered (NH4)2V6O16·1.5H2O nanobelts as a high-performance cathode for aqueous zinc-ion batteries. *Journal of Materials Chemistry A* **2019,** *7* (32), 19130-19139.

(53) Wei, T.; Li, Q.; Yang, G.; Wang, C. Highly reversible and long-life cycling aqueous zinc-ion battery based on ultrathin (NH 4) 2 V 10 O 25· 8H 2 O nanobelts. *Journal of Materials Chemistry A* **2018,** *6* (41), 20402-20410.

(54) Zhang, L.; Chen, L.; Zhou, X.; Liu, Z. Towards High‐Voltage Aqueous Metal‐Ion Batteries Beyond 1.5 V: The Zinc/Zinc Hexacyanoferrate System. *Advanced Energy Materials* **2015,** *5* (2), 1400930.

(55) Trócoli, R.; La Mantia, F. An Aqueous Zinc‐Ion Battery Based on Copper Hexacyanoferrate. *ChemSusChem* **2015,** *8* (3), 481-485.

(56) Zhang, N.; Jia, M.; Dong, Y.; Wang, Y.; Xu, J.; Liu, Y.; Jiao, L.; Cheng, F. Hydrated Layered Vanadium Oxide as a Highly Reversible Cathode for Rechargeable Aqueous Zinc Batteries. *Advanced Functional Materials* **2019,** *29* (10), 1807331.

(57) Wan, F.; Zhang, L.; Wang, X.; Bi, S.; Niu, Z.; Chen, J. An Aqueous Rechargeable Zinc‐Organic Battery with Hybrid Mechanism. *Advanced Functional Materials* **2018,** *28* (45), 1804975.

(58) Kundu, D.; Vajargah, S. H.; Wan, L.; Adams, B.; Prendergast, D.; Nazar, L. F. Aqueous vs. nonaqueous Zn-ion batteries: consequences of the desolvation penalty at the interface. *Energy & Environmental Science* **2018,** *11* (4), 881-892.

Vita

Jianwei Lai received his Bachelor's degree of Energy Chemical Engineering from South China University of Technology in 2017. He is currently a M.S. student in the Department of Mechanical & Industrial Engineering at Louisiana State University (LSU) under the supervision of Prof. Ying Wang. His research interests include the ration design and development of advanced cathode materials for rechargeable aqueous and quasi-solid-state zinc ion batteries. Jianwei Lai's publications and attended conferences during LSU are listed as follows:

1. **J. Lai**, H. Tang, X. Zhu, Y. Wang. Hydrated $NH_4V_3O_8$ Nanobelts Electrode for Superior Aqueous and Quasi-Solid-State Zinc Ion Batteries. *Journal of Materials Chemistry A*, **2019**, DOI: 10.1039/C9TA07822C.

2. **J. Lai**, H. Zhu, X. Zhu, H. Koritala, Y. Wang. Interlayer-Expanded $V_6O_{13}{\cdot}nH_2O$ Architecture Constructed for Advanced Rechargeable Aqueous Zinc Ion Battery. *ACS Applied Energy Materials*, **2019**, 2, 3, 1988-1996.

3. Z. Xie, **J. Lai**, X. Zhu, Y. Wang. Green Synthesis of Vanadate Nanobelts at Room Temperature for Superior Aqueous Rechargeable Zinc-Ion Batteries. *ACS Applied Energy Materials*, **2018**, 1, 11, 6401-6408.

4. **J. Lai**, Y. Wang. Hydrated Ammonium Vanadate Nanobelts Cathode Constructed for High-Performance Rechargeable Aqueous Zinc Ion Battery. *18th Mechanical & Industrial Engineering Graduate Student Conference*, Louisiana State University, Baton Rouge, LA, April 6, 2019 (Oral presentation).

5. **J. Lai**, H. Zhu, X. Zhu, H. Koritala, Y. Wang. High-Performance Aqueous Rechargeable Zinc Ion Battery Based on Interlayer-Expanded $V_6O_{13}{\cdot}nH_2O$ Ultrathin Nanosheets Cathode. *ASME MEED Leadership Summit*, New Orleans, LA, March 21, 2019 (Poster presentation).